Patterns and drivers of peat topographic changes determined from Structure-from-Motion photogrammetry at field plot and laboratory scales

Running head: Patterns and drivers of peat erosion using SfM

Changjia Li*, Richard Grayson, Mark Smith and Joseph Holden

water@leeds, School of Geography, University of Leeds, Leeds, LS2 9JT, UK.

*Correspondence to: Changjia Li, School of Geography, University of Leeds, Leeds, LS2 9JT, UK. E-mail: gycl@leeds.ac.uk; changjia.li@hotmail.com

Highlights

1. Topographic changes, spatial patterns and topographic drivers were investigated by SfM surveys.
2. A net topographic change of –14 to +30 mm yr^{-1} was observed for field peat plots.
3. Freeze–thaw processes first caused net surface topographic rise, with lowering afterwards.
4. Desiccation led to a corresponding surface lowering.
5. Peat losses from laboratory plots quantified by sediment fluxes were seven times smaller than the magnitude of net aerial topographic change calculated with SfM.

Abstract

Little is known about the spatial and temporal variability of peat erosion nor some of its topographic and weather-related drivers. We present field and laboratory observations of peat erosion using Structure-from-Motion (SfM) photogrammetry. Over a 12 month period, 11 repeated SfM surveys were conducted on four geomorphological sites of 18–28 m^2 (peat hagg, gully wall, riparian area and gully head) in a blanket peatland in northern England. A net topographic change of –14 to +30 mm yr^{-1} for the four sites was observed during the whole monitoring period. Cold conditions in the winter of 2016 resulted in highly variable volume change (net surface topographic rise first and lowering afterwards) via freeze–thaw processes. Long periods of dry conditions in the summer of 2017 led to desiccation and drying and cracking of the peat surface and a corresponding surface lowering. Topographic changes were mainly observed over short-term intervals when intense rainfall, flow wash, needle-ice production or surface desiccation was observed. In the laboratory, we applied rainfall simulations on peat blocks and compared the peat losses quantified by traditional sediment flux measurements with SfM derived topographic data. The magnitude of topographic change determined by SfM (mean value: 0.7 mm, SD: 4.3 mm) was very different to the areal average determined by the sediment yield from the block (mean value: –0.1 mm, SD: 0.1 mm). Topographic controls on spatial patterns of topographic change were illustrated from both field and laboratory surveys. Roughness was positively correlated to positive topographic change and was negatively correlated to negative topographic change at field plot scale and laboratory macroscale. Overall, the importance of event-scale change and the direct relationship between surface roughness and the rate of topographic

change are important characteristics which we suggest are generalizable to other environments.

KEYWORDS: peatlands; SfM; topographic change; topographic variables; roughness

Introduction

Peatlands cover approximately 2.84% of global land area (Xu et al., 2018) while storing one third to one half of the world's soil carbon (Yu, 2012). They are globally important for providing various other ecosystem services including those associated with water, food, fibre and leisure (Bonn et al., 2016). Most of these sorts of services are impaired by accelerated peat erosion (Evans and Lindsay, 2010b). Of particular concern is erosion of blanket peatlands which are rain-fed and occur on sloping terrain and thus are potentially more vulnerable to water erosion than other peatland types (Li et al., 2017). Disturbance such as atmospheric pollution, grazing pressure or fire can remove sensitive vegetation which can be followed by rapid incision (Evans and Warburton, 2007). Many blanket peatlands in the Northern Hemisphere have experienced severe erosion (Evans and Warburton, 2007, Grayson et al., 2012, Li et al., 2016b) and are under increasing erosion risk from future climate change (Li et al., 2016a, Li et al., 2017) which will enhance losses of terrestrial carbon in many regions.

The main erosion processes affecting blanket peatlands include sediment supply processes such as freeze–thaw and desiccation, and sediment transport by running water via interrill and gully erosion (Bower, 1961, Evans and Warburton, 2007, Li et al., 2018c, Li et al., 2018b, Li et al., 2018a). Freezing and thawing of water between peat particles is common in cool, high latitude or high altitude climates which support many peatlands, and plays a vital role in breaking up the peat surface during winter months (Francis, 1990, Labadz et al., 1991, Evans and Warburton, 2007, Li et al., 2018b). Surface desiccation during extended periods of dry weather is another important weathering process for producing erodible peat (Burt and Gardiner, 1984, Evans et al., 1999, Francis, 1990, Holden and Burt, 2002a). Interrill erosion is an important process acting at the hillslope scale in blanket peatlands (Bower, 1961) and is a major source of peat and particulate carbon loss where vegetation has been damaged (Grayson et al., 2012). In addition, incision of deep gully systems into the peat surface is an extensive feature in many eroded peatlands (Bower, 1961, Evans and Warburton, 2007). Previous studies have highlighted the role of gully development and its contribution to the overall sediment yield (Evans et al., 2006, Evans and Warburton, 2007, Evans and Lindsay, 2010a).

Numerous direct and indirect methods have been used to measure peat erosion, including erosion pins (Evans and Warburton, 2005) and bounded plots (Holden et al., 2008, Li et al., 2018c, Li et al., 2018b), and more recently modern high resolution topographic surveying methods to improve quantification of erosion (Evans and Lindsay, 2010a, Rothwell et al., 2010, Evans and Lindsay, 2010b, Grayson et al., 2012, Glendell et al., 2017). Erosion plots are used commonly to measure soil erosion over short and medium time periods (Iserloh et al., 2013, Martínez-Murillo et al., 2013) and have previously been applied to peatlands (e.g. Holden and Burt (2002a), Grayson et al. (2012), Li et al. (2018c)). Bounded plots are usually equipped with troughs or sediment collectors to catch exported sediment directly under natural precipitation or rainfall simulations (Holden and Burt, 2002a, Holden and Burt, 2002b, Holden and Burt, 2003, Holden et al., 2008, Li et al., 2018c, Li et al., 2018b, Kløve, 1998). While plot scale or catchment yield studies have supported understanding of peat erosion they usually allow the measurement of the soil loss reaching the plot or catchment outlet, which is then averaged for the entire plot area (Parsons et al., 2006b). The data integrate all upslope processes at a single point (Smith and Vericat, 2015). It is difficult to assess the spatial variation of erosion and deposition and the drivers within the plot due to the lack of sufficient data. Direct measurements of surface denudation with high accuracy would therefore be preferable if we are to understand more about erosion processes.

Remote sensing techniques such as terrestrial laser scanning and digital photogrammetry provide an alternative to erosion plots by constructing 3D surfaces at set intervals and estimating the differences between these surfaces (Smith et al., 2016). Several studies have applied high resolution airborne LiDAR digital elevation models (DEMs) in combination with digital terrain analysis to identify and map landscape features, such as the extent of gully erosion in blanket peatlands (Rothwell et al., 2010, Evans and Lindsay, 2010a, Evans and Lindsay, 2010b, Evans et al., 2005). Grayson et al. (2012) examined the performance of terrestrial laser scanners (ground-based LiDAR) in measuring peat surface retreat rate, and found that terrestrial laser scanning i) allows accurate measurements of the volume of peat lost (or gained) over time at particular test points and ii) provided high resolution spatial data on surface elevation change. However, the use of these remote sensing techniques appears to be limited by high expense and time required for set up (Morgan et al., 2017, Smith et al., 2016).

In recent years, automatic photogrammetric procedures based on SfM and Multi-View Stereo techniques (SfM-MVS) have been widely used in mapping erosion and quantifying their magnitude both in the field and in the laboratory (Prosdocimi et al., 2017, Glendell et al., 2017, Smith et al., 2016, Smith and Vericat, 2015, Micheletti et al., 2015b, Micheletti et al., 2015a, Eltner et al., 2017, Kaiser et al., 2014, Stöcker et al., 2015). However, to the best of our knowledge, there are only two studies that have been reported using and testing the application of SfM techniques in peatlands. Glendell et al. (2017) compared the cost-effectiveness and accuracy of terrestrial laser scanning, aerial (UAV-SfM) and ground-based SfM photogrammetry (GB-SfM) in quantifying the extent of gully erosion in upland landscapes. They found that GB-SfM was the best of the three techniques at measuring the volumes of erosion features at fine spatial resolution. Smith and Warburton (2018) used ground-based SfM surveys to quantify roughness for different peat surfaces and found that SfM was reliable to identify roughness signatures over bare peat plots (< 1 m^2). However, despite the application of new peat surveying techniques there has been a lack of their use to specifically understand spatial and temporal peat erosion dynamics or processes in a range of peatland environments.

This study aims to apply SfM topographic reconstruction to study dominant peat erosion processes at field plot and laboratory macro scales. The specific objectives are to:

(i) Examine the spatial and temporal variability of topographic change patterns on peat erosion sites using repeat SfM surveys.

(ii) Investigate erosional-depositional processes and their controlling topographic and weather-related drivers.

(iii) Compare peat interrill erosion rates determined by laboratory plot sediment flux and by SfM photogrammetry.

Material and methods

Field experiments

Study area

Extensive peat erosion in the UK occurs across many blanket peatlands, especially in the Pennine region of England (Bower, 1960a, Bower, 1961, Evans and Warburton, 2007). Fleet Moss (SD 86 83; 54°07´N, 2°16´W) is an area of approximately 1.0 km^2 with deep upland blanket peat at an altitude of 550–580m in the Yorkshire Dales, England (Figure 1 (a)). The study area is a mini-catchment within Fleet Moss, with a large area of exposed bare peat actively eroding with sheet erosion and gullying. There are well developed and connected Type 1 and Type 2 gully systems (Li et al., 2018a): Type 1 dissection usually occurs on the flatter interfluve areas where peat is usually 1.5–2.0 m in depth on slopes less than 5° (Bower, 1960a), with gullies frequently branching and intersecting as an intricate dendritic network; Type 2 dissection dominates on steeper slopes (exceeding 5°), with a system of sparsely branched drainage gullies incised through the peat and aligned nearly parallel to each other. The vegetation is dominated primarily by Eriophorum vaginatum, Calluna vulgaris and Empetrum nigrum.

Four field sites across Fleet Moss with different types of erosion features were selected for survey (Figure 1). The peat hagg (Site 1) was an erosional escarpment with different active processes occurring in different positions (Evans and Warburton, 2007). Slump, saltation and lateral rain and wind impact are likely dominant on the upper slope; sheet wash and needle ice and freeze–thaw are probably dominant on the middle slope; while saltation and rill development are more likely along the lower slope (Evans and Warburton, 2007). Site 2 is a lateral-bank headcut on a gully wall for a ‘V’ shaped gully profile (Bower, 1960a), and Site 4 is a main headcut of the gully. Both Site 2 and Site 4 are characterized by Type II gully erosion that has unbranched channels aligned normal to the slope on steeper ground with a mean slope gradient above 17° (Bower, 1960b). Site 3 is a flat toeslope area adjacent to the stream.

< Figure 1 is here >

Data acquisition

Weather data

Precipitation was measured by a digital tipping bucket raingauge at 15–minute intervals from 15/10/2016 to 15/11/2017 (Figure 2 (a)). Temperature loggers (Tinytag Plus 2) were used at the peat surface recording at 10–minute intervals from 26/10/2016 to 20/07/2017 (Figure 2 (b)). Temperature data was not recorded since 20/07/2017 due to malfunctioning loggers. Mean annual rainfall at a nearby long-term rain gauge at Snaizeholme (54°17´20´´N, 2°15´28´´W and 260 m altitude) is 1740 mm (1961–2017) with a maximum of 2667 mm and minimum of 1296 mm (UK National River Flow Archive, 2018). Rainfall during 2016 was 1655 mm at Snaizeholme and 1723 mm in 2017. Our own gauge at Fleet Moss (570 m altitude) recorded 1997 mm between 1 November 2016 and 31 October 2017 while the value was 1677 mm for Snaizeholme. While spring 2017 rainfall (329 mm at Fleet Moss) was close to the long-term Snaizeholme mean value of 319 mm, there was a dry period between 1 April and 12 May with only 23.2 mm. During 2017 the mean annual temperature for the Yorkshire Dales where Fleet Moss is located was 0.2–0.5 ºC greater than the 30-year annual mean (1981–2010). Spring 2017 was substantially warmer with a mean temperature 1.0–1.5 ºC greater than that of the 1981–2010 average (UK Met Office, 2018).

< Figure 2 is here >

SfM Photogrammetry

SfM photogrammetry calculates three-dimensional (3D) surface models from 2D images via a workflow comprising: (i) keypoint detection and matching; (ii) bundle adjustment algorithms to identify scene geometry and camera interior and exterior parameters simultaneously; (iii) georeferencing using control points identified in imagery and application of a standard seven-parameter rigid body transform; and (iv) application of multi-view stereo image matching algorithms to yield the final dense point cloud. For full details of the SfM workflow see James and Robson (2012) and Smith et al. (2016). An object of interest is observed from overlapping images acquired from different positions. From 26/10/2016 to 02/11/2017, the four sites were surveyed 11 times (Figure 1(a)). Weather conditions during field campaigns can significantly influence data quality (Snapir et al., 2014, Stöcker et al., 2015). Image acquisition was mainly conducted under conditions with no strong wind, rain or snow cover. However, sunny weather during the November campaign (04/11/2016) produced images with shadows that resulted in decreasing contrast and some data gaps where no image points could be extracted. For the other 10 field campaigns, data acquisition was arranged to avoid sunny conditions in order to enable diffuse illumination conditions and minimize shadows.

Abundant high quality images were subsequently taken at positions and angles that have sufficient coverage of the peat erosion features of interest. In specific erosion features (i.e. gully heads, peat hagg), the density of images from additional perspectives was increased for further detailed reconstruction. The camera used was a Sony ILCE-6000 24 mega pixel digital camera with a 16 mm focal length.

Camera settings varied based on light conditions, with exposure between 160 and 320 ISO, F-stop between f/4 and f/4.5 and exposure time between 1/160 and 1/80 second.

Between 8 and 12 permanent Ground Control Points (GCPs) made of rebar (0.5–1.0 m in length) were placed around and within each feature (Figure 1 (d) and Table 1). The rebar was hammered deep into the substrate below the peat with a painted white top (high contrast with the dark peat surface). A geodimeter was used and full surveys of the relative coordinates of all the GCPs were carried out at the start of the monitoring period.

< Table 1 is here >

Laboratory experiments

Material

Bare peat blocks were collected from the upper peat layer at Moor House National Nature Reserve (NNR) (54°41’N, 2°23’W), a blanket peat site in the North Pennines of England. A plastic rectangular gutter (1.0 m long, 0.13 m wide and 0.08 m in depth) was pushed into the peat parallel to the peat surface, and carefully dug out to extract an undisturbed peat block. All samples were tightly sealed using plastic film to minimize peat oxidation and drying before being stored at 4℃ prior to laboratory analysis. Basic chemical and physical properties of the peat blocks were determined on subsampled peat (Li et al., 2018c).

The experiment used a ‘drip-type’ rainfall simulator (Bowyer-Bower and Burt, 1989, Holden and Burt, 2002a), a Mariotte bottle located at the upslope plot boundary to provide upslope inflow at a constant rate and a 1.0 m long by 0.13 m wide soil flume.

The general set-ups and operating principles of the rainfall simulator, inflow device and soil flume are illustrated in Li et al. (2018c).

Experimental design

For interrill erosion on gentle peat slopes, peat particle detachment and transport are simultaneously influenced by rainfall-driven and flow-driven erosion processes and their interaction (Li et al., 2018c). In this study, the slopes were set at 2.5° and 7.5° to represent either side of the transition (5°) between Type 1 (heavily branching) and Type 2 (linear) dissection of gully systems (Bower, 1960a) and also being representative of typical blanket peatland slopes in the Pennine region of England. For each slope gradient, three treatments were conducted on the bare peat blocks (Table 2):

(i) Rainfall events to simulate rainfall-driven erosion processes: Rainfall was applied at an intensity of 12 mm hr^{-1} for a duration of 120 min.

(ii) Inflow events to simulate flow-driven erosion processes: Upslope inflow was applied with a constant rate of 12 mm hr^{-1} determined by a volumetric method and which corresponded to 12 mm hr^{-1} rainfall on the studied plots.

(iii) Rainfall + Inflow events to simulate the combined impacts of rainfall and flow on erosion processes. Both rainfall (12 mm hr^{-1}) and upslope inflow (12 mm hr^{-1}) were applied simultaneously.

< Table 2 is here >

Data acquisition

Sediment flux method

During each run the time of overland flow-initiation was recorded, after which each test lasted for 120 minutes. Total surface overland flow was sampled at the plot outlet every 5 minutes. Overland flow volumes for each sample were determined using a measuring cylinder. Overland flow rates (mL s^{-1}) were subsequently determined by dividing these overland flow volumes by the sampling duration. Samples were then left to settle for six hours to allow deposition of the suspended sediment. The clear supernatant was decanted, and the remaining turbid liquid was transferred to a rectangular foil container and oven-dried at 65.0℃ until a constant weight was achieved. The dry sediment mass (in milligrams) was calculated, and the sediment concentration (in mg mL^{-1}) was determined as the ratio of dry sediment mass to the overland flow volume. The sediment yield rate (in mg m^{-2} s^{-1}) was defined as the ratio of dry sediment mass per unit area per sampling duration. The sediment flux data on peat blocks was reported in Li et al. (2018c) which provides a data set for comparison with the laboratory scale SfM data which is, for the first time, presented in this new paper.

SfM Photogrammetry

In addition to the sediment flux approach, high resolution topographic data derived from SfM photogrammetry was acquired before and after each rainfall simulation experiment. Overlapping oblique 2D images of each plot, pre- and post-event, were taken using a FUJIFILM FinePix AX650 16 mega pixel digital camera with focal length set at 6 mm and with automatic exposure enabled. 23 GCPs were positioned along the boundaries of the flume and were marked with high-visibility markers. A local co-ordinate system was used and the relative co-ordinates of the 23 GCPs were determined by measurements and geometric calculation.

< Table 3 is here >

Data analysis

SfM data processing

Images acquired were processed using the commercial software Agisoft PhotoScan. First, image quality was checked visually and by estimating image quality through Photoscan. Any blurred images or those with a quality score < 0.5 were removed. Second, photographs were aligned to produce a sparse point cloud and the default setting with the photo alignment accuracy was set to “highest”. Tie points were refined by gradual selection in Photoscan based on criteria of “reprojection error” and “reconstruction uncertainty”. Third, GCPs were identified in each photograph to georeference the sparse cloud. The residual georeferencing errors were calculated and point-cloud quality was evaluated by summarizing residual errors using root mean squared error (RMSE) (Smith et al., 2014). Poorly located GCPs were excluded; however, a minimum of six GCPs that were well distributed over each site remained (Fonstad et al., 2013, Smith et al., 2014). Mean georeferencing uncertainty in the final point clouds was 0.033 m for the field data (RMSE; Table 1) and was 0.005 m for the laboratory data (RMSE; Table 3). Fourth, a dense point cloud was subsequently produced using PhotoScan’s multiview stereo (MVS) algorithm. Dense cloud quality was set to “Highest” for laboratory data processing and “medium” for field data processing as a compromise between model quality and processing time. The dense cloud was subsequently edited to remove noise points such as those not on solid surfaces.

Point cloud differencing

Lague et al. (2013) provided a detailed review of the main advantages and drawbacks of the approaches normally used (e.g., DEM of difference, C2C, M3C2) to measure the distance between two point clouds. In our study the Cloud-to-cloud differencing was computed using the Multiscale Model to Model Cloud Comparison (M3C2) algorithm due to its ability to quantify the 3-D distance between two point clouds along the normal surface direction and provide a 95% confidence interval based on the point cloud roughness and co-registration uncertainty (Lague et al., 2013). The M3C2 tool is available in the open source CloudCompare software and has been widely used in a range of environments (Lague et al., 2013, Watson et al., 2017, Mallalieu et al., 2017, Barnhart and Crosby, 2013, Gómez-Gutiérrez et al., 2015, Stumpf et al., 2015, Morgan et al., 2017). The general concept behind M3C2 is to compute Cloud 1 to Cloud 2 distances using a local normal direction that is defined by fitting a plane to all of the points within a sphere that has a diameter D (the 'normal diameter') around a given core point i. Once the point normal direction is computed, the algorithm subsequently creates a cylinder oriented along the normal direction, with a diameter d (the 'projection diameter') specified by the user. All of the points in Cloud 1 and Cloud 2 that reside in the cylinder are spatially averaged to determine mean surface positions, i_1 and i_2, respectively. L_{M3C2} is the distance between i_1 and i_2 and is stored as an attribute of i (Lague et al., 2013).

M3C2 requires users to define two main parameters: i) the normal scale D, which is used to calculate a surface normal for each point and is dependent upon surface roughness and registration error; ii) the projection scale d within which the average surface elevation of each cloud is calculated. In this study, the normal scale D for each point cloud was estimated based on a trial-and-error approach similar to that of Westoby et al. (2016), to reduce the estimated normal error, E_{norm} (%), through refinement of a rescaled measure of the normal scale n(i):

$$n(i) = \frac{D}{\sigma_i(D)} \quad (1)$$

where n(i) is the normal scale D divided by the roughness σ measured at the same scale around i. and where n(i) falls in the range 20–25, E_{norm} < 2% (Lague et al., 2013). In this study for the field data processing, normal scale D ranged from 0.3 to 0.5 m and projection scale d was specified as 0.1 m and this scaling was enough to average a minimum of 30 points sampled in each cloud (Lague et al., 2013). For the laboratory data processing, normal scale D was fixed at 0.05 m and projection scale d was specified as 0.005 m.

Cloud-to-cloud distance was projected onto the original point cloud. In addition to the distance, M3C2 reports the number of points within the projection cylinder (a measure of local point density) and the standard deviation of the points within the cylinder (a measure of local roughness). A spatially variable confidence interval (SVCI) was proposed to account for the precision of the M3C2 distance affected by the local point density, roughness and the registration error (Lague et al., 2013). M3C2 output was subsequently masked to exclude points where change is lower than Level of Detection (LoD) threshold for a 95% confidence level, which is defined as:

$$LOD_{95\%}(d) = \pm 1.96(\sqrt{\frac{\sigma_1(d)^2}{n_1} + \frac{\sigma_2(d)^2}{n_2}} + reg) \quad (2)$$

where σ_1 and σ_2 represent the roughness of each point in sub-clouds of diameter d and size n_1 and n_2, and reg is the user-specified registration error which is assumed to be isotropic and spatially uniform across the dataset (Lague et al., 2013). The surface-to-surface Interactive Closest Point algorithm implemented in CloudCompare was used to align a patch of two inactive point clouds. The registration error was estimated by a series of tests, and it ranged from 4.5 mm to 5.0 mm for the field models and ranged from 0.7 mm to 0.8 mm for the laboratory models. Distance calculations were masked to exclude points where the change was lower than the $LoD_{95\%}$ threshold.

For each field site, data analyses were conducted on two temporal scales: (a) between individual survey dates and (b) longer-term seasonal to annual change. Survey dates and intervals are presented in Table 4. Between 26/10/2016 and 02/11/2017 the 11 repeat topographic surveys yielded 10 short-term survey intervals (e.g., 2–1; 3–2) and a long-term survey interval (11–1). The length of the short-term scale survey intervals ranged from 10 days (26/10/2016–04/11/2016) to 69 days (13/06/2017–21/08/2017). The long-term survey interval was selected to represent potential large topographic changes.

Other data analysis

For all points with calculated M3C2 distance above the LoD threshold at 95% confidence level, topographic variables were analyzed for statistical relationships with observed M3C2 changes. The topographic variables examined were aspect, slope, curvature, profile curvature, plan curvature and roughness; these variables were derived from surface analyst tools in ArcGIS 10.4 based on DEM deriving from point clouds gridded at 0.01 m for field models and 0.001 m for laboratory models. The variables were extracted to point datasets that were tested for normality using the Anderson–Darling normality test. Spearman's rank correlation and stepwise regression were used to test for relationships between topographic factors and topographic change.

Six meteorological variables were calculated to determine the meteorological influence on observed temporal variability of topographic change for field short-term surveys. The calculated variables included: (i) number of days between SfM surveys, (ii) number of rainy days, (iii) total rainfall (mm), (iv) maximum 15–minute rainfall intensity, (v) mean temperature and (vi) number of days below freezing (i.e. 0 ℃; calculated as the number of days in which at least one value below 0 ℃ was registered in the 10–minute interval temperature data set) and (vi) number of frost cycles. Datasets were tested for normality using the Anderson–Darling normality test and the Spearman's rank correlation was used to find the relationship between meteorological variables and topographic changes.

Results

Field results

M3C2 differences of peat surface from multi-temporal field surveys

M3C2 differences above Level of Detection threshold at 95% confidence level ($LoD_{95\%}$) over different survey intervals are given in Table 4. Net topographic changes estimated for the whole study period were highly variable. A net negative topographic change was monitored in the peat hagg (Site 1, Model 11–1, median = 14 mm, RMS = 19 mm) and the peat gully wall (Site 2, Model 11–1, median = 13 mm, RMS = 23 mm). In contrast, a net positive topographic change was monitored in the riparian area (Site 3, Model 11–1, median = 30 mm, RMS = 35 mm) and the peat gully head (Site 4, Model 9–1, median = 22 mm, RMS = 29 mm) (Table 4).

From 26/10/2016 to 04/11/2016, the net topographic change was negative for the Site 1, 2 and 3 (Model 2–1), but was positive for the Site 4 (Model 2–1). During the period of 04/11/2016–30/11/2016, the peat surface for Sites 1, 2 and 3 experienced a positive net topographic change, with a median net increase in the surface height of 14, 18 and 17 mm, respectively. There was a positive net topographic change for Sites 1, 2 and 3 from 21/12/2016 to 22/02/2016 (Model 5–4). However, a net negative topographic change was monitored for all four sites over the period of 22/02/2017–07/04/2017 (Model 6–5 for Sites 1, 2 and 3, and Model 4–3 for Site 4).

< Table 4 is here >

Top view on the features of interest was shown in Figure 3. The spatial distribution and histogram of M3C2 differences for short-term and long-term comparisons are shown in Figure 4 through Figure 7. M3C2 distances ranged from negative values (red colour) that showed eroded sediment, to positive values (blue colour) that indicated deposited sediment. Topographic changes were mainly observed over short-term intervals when intense rainfall (i.e. Figure 6 (j)), flow wash (i.e. Figure 4 (a) and Figure 5 (a)), needle-ice production (i.e. Figure 4 (b), Figure 5 (b) and Figure 6 (b)), surface desiccation (i.e. Figure 4 (e) and Figure 5 (e)) or surface swelling (i.e. Figure 7 (a)) was observed. On 30/11/2016 field survey showed that needle-ice was formed within the upper layer of the peat surface on Site 1 (hagg), Site 2 (gully wall) and Site 3 (riparian area) (Table 1). As a result the calculated M3C2 distance showed positive values across the three sites (Figure 4 (b), Figure 5 (b) and Figure 6 (b)). Drying and cracking of the peat surface was observed during the field campaign on 07/04/2017, resulting in a negative topographic change across the field sites (Figure 4 (e), Figure 5 (e) and Figure 7 (c)). Water recharging and surface welling processes were evident on Site 4 (gully headcut) during the survey on 04/11/2016, leading to positive topographic change across much of the site (Figure 7 (a)).

< Figure 3 is here >

< Figure 4 is here >

< Figure 5 is here >

< Figure 6 is here >

< Figure 7 is here >

Relationships between spatial patterns and topographic variables

Aspect, slope and surface roughness were the most significantly correlated topographic variables for almost all of the topographic changes (Table 5). Although statistically significant for many intervals, neither curvature nor plan curvature were the most significant predictor of topographic change in any survey interval. Profile curvature was the most significant topographic predictor only for Site 2, Model 9–8.

For the positive topographic changes, roughness was positively correlated to M3C2 distance; while for the negative topographic changes, roughness was negatively correlated to M3C2 distance (Table 5). This relationship is presented in more detail in Figure 8 (a–b) where the effect of roughness on topographic change is evident. These results suggest that rougher cells are indicative of more active topographic change. The Spearman's rank topographic change – roughness correlation coefficients for the short-term surveys were generally greater than those of the long-term surveys. For example, Model 4–3 (Site 1) had coefficient of 0.555 and 0.529 for the correlation between roughness and total and positive topographic changes, respectively, compared to 0.280 and 0.315 produced by Model 11–1 (Table 5). Slope had strong negative correlations with negative topographic change

(Table 6), indicating that erosion increases with an increase in slope gradient (Figure 8 (c)).

< Table 5 is here >

< Figure 8 is here >

Relationships between meteorological variables and topographic change

Meteorological variables for different survey intervals are presented in Table 6. A total of 2012.0 mm of precipitation, mainly of long-duration and low intensity, was recorded on 266 days during the whole 373 day survey period (Table 6). Maximum 15–minute rainfall intensity ranged from 0.2 mm to 7.2 mm. Mean temperature during the period of 04/11/2016–30/11/2016 was lowest (1.5 ºC), and it gradually increased from 22/02/2017. The winter of 2016 had 38 freezing days with sub-zero temperatures recorded.

< Table 6 is here >

Spearman's rank correlations between the six meteorological variables and median net, positive and negative topographic changes showed that the relationships were generally not significant ($p > 0.05$). However, on the gully head (Site 4) negative topographic change was significantly correlated with total rainfall ($p < 0.05$). Further regression analysis (Figure 9) showed that a linear relationship ($y = -0.0011x - 1.1969$, $n = 8$, $R^2 = 0.519$, $p < 0.05$) performed well in describing the relationship between topographic change (y) and total rainfall (x) for Site 4.

< Figure 9 is here >

Laboratory results

M3C2 differences of peat surface

The georeferencing errors calculated by the Agisoft Photoscan software ranged from 4.2 to 5.6 mm under the laboratory conditions (Table 3). M3C2 differences above Level of Detection threshold at 95% confidence level for different treatments are given in Table 7. The net median topographic change ranged from –5 mm to 5 mm (Table 7). In general a net negative topographic change was monitored for the Rainfall and Rainfall + Inflow treatments; in contrast, a net positive topographic change was monitored for the Inflow treatments (Table 7).

< Table 7 is here >

Figure 10 gives the spatial patterns of the significant M3C2 distances (> LoD 95%) and histograms of the differences. Some treatments (e.g., 2.5°R1, 2.5°RF1, 7. 5°R2 and 7.5°RF2) mainly show negative topographic changes while others (e.g., 2.5°F1, 7.5°R1 , 7.5°F1 and 7.5°F2) show greater positive topographic changes (Figure 10). These results suggest that simulated rainfall and simulated rainfall + inflow events cause both spatially distributed erosion and deposition as captured by SfM. However, the simulated inflow events had positive topographic changes under both the 2.5° and 7.5° conditions.

< Figure 10 is here >

Comparison of peat erosion rates measured by SfM and sediment fluxes

Figure 11 shows the peat loss data, expressed in grams, derived from both the sediment fluxes and SfM methods. Only erosion was measured by the sediment flux method and the total amount of peat loss (dry weight) ranged from 0.26 g to 2.43 g for different treatments. However, both positive and negative topographic changes were found for the SfM technique, indicating spatially distributed erosion / deposition patterns. The SfM method resulted in an estimated mean peat deposition rate of 7.02 g (0.7 mm topographic change), with standard deviation as48.29 g (4.3 mm), compared with a mean peat loss rate of 1.05 g (0.1 mm), with standard deviation as 0.55 g (0.1 mm) derived from the sediment fluxes. The standard deviation of mean topographic change measured by the SfM method was much greater than the sediment flux method, showing a much greater magnitude of topographic change. From the figures showing M3C2 distances and histogram of differences (Figure 11), there were areas with both positive and negative topographic changes on the peat block and these features were well described by the SfM method.

< Figure 11 is here >

Relationships between spatial patterns and topographic variables

The Spearman's rank correlation coefficients are presented in Table 8, with the most significant topographic factors highlighted in bold. For all of the M3C2 comparisons curvature, roughness and slope were the most significant topographic variables ($p < 0.01$) (Table 8). Although statistically significant for many models, none of aspect, profile curvature and plan curvature were the most significant predictor of topographic change in any model. Curvature showed significantly negative correlations with topographic change for all three treatments (R, F and RF) demonstrating that topographic change decreased with an increase in curvature.

< Table 8 is here >

For the positive topographic changes, roughness was positively correlated to M3C2 distance; while for the negative topographic changes, roughness was negatively correlated to M3C2 distance (Table 8). This relationship is presented in more detail in Figure 12 (a–b) where the effect of roughness on topographic change is evident. These results suggest that rougher cells are indicative of more active topographic change. Slope showed strong negative correlations with negative topographic change (Table 6), indicating that erosion increases with an increase in slope gradient (Figure 12 (c)).

< Figure 12 is here >

Discussion

SfM reconstructions of topographic changes

Geomorphic processes such as: i) water and aeolian erosion/deposition; ii) freezing and needle ice expansion and desiccation shrinkage; and iii) shrink–swelling and oxidation are operate on peat hillslopes (Grayson et al., 2012, Evans and Warburton, 2007, Glendell et al., 2017). The topographic change measured by the SfM technique is an aggregation of all of these processes across survey areas. In this study the ‘positive M3C2 distance’ reflects topographic change that could be caused by both deposition and swelling processes; while ‘negative M3C2 distance’ could also be attributed to both erosion and shrink processes.

3D reconstruction of topographic changes at plot scale (field experiments)

The error we obtained during the manual registration of the point clouds (mean value of 33 mm) is within the range of registration errors found by other studies in natural terrain (Glendell et al., 2017). Glendell et al. (2017) reported a root mean square error based on GCPs ranging from 11 mm to 291 mm, with a mean value of 46 mm for different types of erosion features. Our study showed that the topographic changes observed over one year ranging from –14 to 30 mm for the four field sites.

These values are moderate in comparison with the globally reported negative topographic change rates (24 ± 8 mm yr^{-1}) measured using erosion pins (Evans and Warburton, 2007, Grayson et al., 2012). Glendell et al. (2017) used ground photography SfM in ten upland peat sites distributed across England and Wales to measure erosion. They found the mean topographic change rate for the gully floor of different sites ranged from –286 mm to 31 mm yr^{-1} and the mean value was –33 mm yr^{-1}.

A net deposition of 30 mm was estimated for a relatively flat bare peat surface (Site 3) for the survey period from 26/10/2016 to 02/11/2017. This result is not in agreement with those previous studies (Imeson, 1974, Tallis and Yalden, 1983, Anderson, 1986) reporting a surface retreat rate of 1–41 mm yr^{-1} on low angled bare peat surfaces from similar blanket peat environments derived from erosion pin data. The discrepancy may be caused by the differences in the geomorphological context or the approaches to measure topographic change. Erosion pins measure erosion or deposition directly through observed changes in the peat surface at a given point (Grayson et al., 2012, Tuukkanen et al., 2016) and the point measurements are subsequently interpolated over relatively small areas. However, significant spatial variation even over small areas (Grayson et al., 2012) affects the accuracy and precision of erosion rates based on erosion pins. In addition, the pin method suffers from problems of disturbance and damage to the peat surface caused by repeated pin measurement. Consequently, erosion pin measurements are typically taken over long time periods to obtain high signal to noise ratio and more meaningful results. SfM is capable of providing fully distributed estimates of topographic change across a large area with minor disturbance of the peat surface. Grayson et al. (2012) compared the use of erosion pin and terrestrial laser scanning techniques for measuring erosion across a peatland site in northern England and found very different erosion rates: a net surface lowering of 38 mm measured using pins but a net deposition of 3–7 mm was calculated from laser scanning. However, SfM is still subject to a wide range of controls on surface elevation over short time periods so that the consideration of signal and noise is still pertinent.

<u>3D reconstruction of topographic changes at plot scale (laboratory experiments)</u>

Both positive and negative topographic changes were observed using SfM for simulated rainfall and simulated rainfall + inflow events. However, only positive topographic changes were captured for simulated inflow events. This means that simulated inflow events appeared to cause a higher net level of deposition-related topographic change than erosional denudation. Our previous studies showed that the effect of shallow overland flow on peat erosion, in the absence of rainfall, was low (Li et al., 2018c). Positive topographic changes could be explained by saturation-related surface upwelling processes pushing peat particles upwards, or more likely it is due to the fact that eroded peat is loose and less compact that when it was in situ and so re-deposition of such loose peat materials could result in positive topographic change.

Peat loss data estimated with sediment fluxes at the plot outlet and SfM methodologies were not comparable with each other (Figure 11). Deposition-related change measured by SfM was 7.02 ± 48.29 g (0.7 ± 4.3 mm), in comparison with erosion-related change derived from the sediment flux method of 1.05 ± 0.55 g (0.1 ± 0.1 mm). The two approaches measure different things and are suitable for different applications. For many applications surface change is used as a proxy for erosion; while for other applications the mass lost is a key parameter of interest.

Spatial and temporal evolution of eroding headwater peatlands

The main headcut of the tributary (Site 4) experienced net accumulation during the whole study period, with a median net increase in the peat surface height of 22 mm (Table 4). This result suggests that incision dynamics and headward migration of the gullies was not active during the whole study period. The main reason is probably that the headcut is covered with dense vegetation on the upper hillslopes (Figure 1), which may limit rapid overland flow and prevents the expansion of the gully network. Negative topographic change mainly occurred at the base of the headcuts due to wash of flow accumulated from upper positions. Among the four study sites, the lateral-bank headcut (Site 2) had the most significant negative topographic changes and net surface lowering for the majority of surveys. Field observations showed that the location of the steep lateral-bank headcut (Site 2) was strongly linked with flowpaths that concentrated and directed overland flow from the upper gentle hillslopes to the main channel (Figure 1), resulting in active progress of gully incision. These results confirm that gully networks can expand rapidly in peatlands (Bower, 1960b). It is thus very important to reduce the hydrological connectivity and slope steepness of gully walls in order to control peatland gully erosion.

A net increase in the peat surface height was observed for the surveyed sites in November 2016 (see Figure 5 (b) for an example). Low temperatures observed during this month (Table 6) were accompanied by significant ice on the surface which led to an expansion of the peat surface. In addition, diurnal freezing was common in November 2016 with temperature frequently fluctuating above and below zero (Figure 2) which was ideal for needle ice growth. Freezing and thawing occurred multiple times and as such was important in producing loose particles and aggregates on the surface. The subsequent rainfall events in December caused erosion of the available peat materials prepared by previous needle-ice freezing and thawing, leading to a net surface lowering (Table 4). These results are in agreement with those reported by Li et al. (2018b) who found that needle ice production is a primary process contributing to upland peat erosion by enhancing peat erodibility during runoff events following thaw. A net decrease in the peat surface height was observed for all four sites from 22/02/2017 to 07/04/2017 (Table 4). Over this period there was a general increase in the mean temperature. The long periods of dry conditions in April 2017 (Table 6) resulted in desiccation and drying and cracking of the peat surface and a corresponding surface lowering. Our study showed that short term topographic changes allow useful inference of processes, which are similar to those reported by Evans and Warburton (2007) based on high temporal resolution measurement of peat surface elevation.

A comparison of consecutive surveys with longer-term survey intervals that integrate multiple events reveals different patterns (Table 3 and Figures 4–7). In this study, the main topographic change was observed between a single short-term interval when intense rainfall, flow wash, needle ice production or surface desiccation was observed. However, several changes observed at the short-term scale were cancelled out by further topographic changes in the opposite direction (i.e. erosion followed by deposition) that cannot be discerned from longer monitoring intervals. When attempting to determine topographic changes and earth surface processes, an event-scale survey resolution that can capture important drivers (i.e. heavy rainfall event, needle ice production, serious desiccation) is therefore important. The stronger control of roughness observed at the event-scale exemplifies the importance of event-scale monitoring. These results obtained from upland peatlands, are in agreement with those reported by Vericat et al. (2014) in a humid badland, who found that an event-scale survey resolution was important for detecting geomorphological changes and could yield better understanding of the driving processes than long-term survey intervals which integrate over multiple process-responses making individual drivers more difficult to determine.

Relationships between spatial patterns and topographic variables

From the relationships identified between spatial patterns of topographic change and topographic variables, there are four key factors that should be highlighted. First, a significant relationship between topographic change and surface roughness was observed consistently at both the field plot scale (Table 5) and laboratory macroscale (Table 8). Roughness was positively correlated to the positive topographic change; while was negatively correlated to negative topographic change. The main reasons are: i) an increased roughness of bare peat surfaces has important feedbacks on sediment transport mechanisms by reducing overland flow velocity; and ii) surface roughness at the studied small scales provides insights into the erosion agents (e.g., wind-driven rain, surface wash, frost action and desiccation) and the relative magnitude and direction of the sediment transfer process (Evans and Warburton, 2007, Smith and Warburton, 2018). In addition, this study highlights the importance of roughness in particular for short-term surveys during which needle-ice production, desiccation and rainsplash and surface wash take place. Over the long-term scale the relationship was less pronounced. The main reason is probably that both the topographic change and roughness of bare peat surfaces are driven by key natural drivers (rainfall, surface wash, wind action, needle-ice production and desiccation) that take place at event-scales (Evans and Warburton, 2007, Smith and Warburton, 2018). However, as roughness changes soon after the initial survey, over longer timescales topographic changes are less strongly related to initial roughness and other topographic variables (i.e. slope or aspect) become more important (Table 5, see Model 11–1 for an example). Our study is in agreement with Vericat et al. (2014) who found via a series of event-scale surveys that roughness had a significant linear relationship with topographic change in a sub-humid, highly erodible badland. From the multi-temporal perspective these studies suggest that roughness is an important factor in the development of humid peatlands and other environments such as sub-humid badlands. In addition, the importance of roughness is enhanced at particular times of year such as during frost events (needle-ice freezing and thawing) in winter, desiccation in a dry summer period and heavy rainfall events in early autumn. Surface roughness controls on spatial patterns of topographic change are also illustrated by laboratory event-scale surveys before and after the rainfall simulation experiments (Table 8). Second, the relationship between slope and topographic change was also important (Figure 8 and 12) and would be expected (Grayson et al., 2012, Fox and Bryan, 2000). The positive correlation of slope with drainage density reflects the dominant role of fluvial action in initiating peat erosion (Mosely, 1972). Third, a significant relationship between curvature and topographic change was evident especially for the laboratory micro peat block scale (Table 8). Fourth, a significant relationship between aspect and topographic change was found at the field plot scale. For some models (i.e. Site 1: Model 5–4) aspect was the main driver of change (Table 6). The west-facing part of the peat hagg was actively eroded, suggesting that the prevailing westerly wind and lateral rain were important processes on the peat hagg (Evans and Warburton, 2007). More needle-ice formation was found during winter months on the north-facing gully wall than the other three field sites.

Implications of SfM applications for peat erosion study

In this study we used SfM photogrammetry for peat laboratory flumes and field sites with different geomorphological features. SfM is a technique that is cheap, fast and easy to use in terms of data acquisition and post-processing. SfM provides fully distributed estimates of topographic change and datasets for quantification of controls and drivers. In addition, SfM has the advantage of removing surface disturbance which is difficult to avoid when using many conventional and invasive methods such as erosion pins.

In future, a more detailed understanding of the processes driving observed erosion and deposition patterns could be informed by a segregation of the sediment budget according to the driving process, achieved either by visual inspection, analysis of localised volumetric changes (Wheaton et al., 2013) or roughness analysis (Smith and Warburton, 2018).

Compared to sediment flux at the outlet of bounded plots, SfM is capable of capturing microscale processes that are important in producing variable topographic change patterns during sheet wash even at the very fine (0.13 m^2) scale. The high-resolution topographic data derived from SfM provides insights into both the quantities and also the potential controls and drivers of such geomorphic changes.

In this study we used permanent GCPs to reduce errors derived from disturbance and damage to the peat during repeat surveying of the coordinates of GCPs. However, future work is required to reduce error for field SfM surveys in peatlands, and for other environments (Borrelli et al., 2017) where erosion or deposition is only a few cm or mm per year.

Numerical models, such as the USLE (May et al., 2010), CAESAR model (Coulthard et al., 2000) and the PESERA–PEAT model (Li et al., 2016b) have been tested in blanket peatlands and are capable of predicting some runoff–erosion relationships. However, incorporating some of the important erosion processes into peat erosion models remains a challenge either due to difficulties in the parametrization of processes that are not fully understood or, as is often the case, a lack of field data for model calibration and validation. Erosion models depend on Digital Elevation Models (DEMs) and their modelling abilities have usually been applied at large-scales (regional, national and global scales) with relatively low resolution DEMs to shorten calculation time. However, since processing time is decreasing with growing computer capacity, there is an increasing trend towards high resolution and small-scale erosion modelling (Kaiser et al., 2014). In this context, the use of SfM techniques provides new possibilities. High resolution DEMs derived from SfM techniques at centimeter-scale or even higher resolution enables sediment budget estimation and erosion features (e.g. rill formation, gully incisions) to be depicted more precisely. The M3C2 and volumetric change data can be used for peat erosion modelling, as predicted peat erosion rate (e.g., surface retreat rate, peat loss volumes) can be validated by SfM measurements.

Limitations

Topographic change in the peat surface can occur through changes in peat density that could result from lower density peat being deposited at the peat surface from upslope, or from swell-shrink and freeze-thaw processes that make the peat less dense at the surface. Future longer (at least annual) timescales of monitoring should be undertaken to capture longer term signals that stand out from the noise of surface oscillations caused by short-term peat density changes.

The size of the peat blocks used in the laboratory was fairly small but meant that it was feasible to obtain undisturbed samples for laboratory treatment, and to produce quantifiable results with good levels of experimental control. However, it should be noted that the bounded plots produce erosion rates declining with rainfall simulation due to the previously weathered peat particles being splashed and transported by overland flow, resulting in a detachment-limited condition (Li et al., 2018c).

The four field survey plots were selected to represent typical erosion features in blanket peatlands. However, peat loss measurements at one scale are not representative of sediment yield at another scale. A direct extrapolation of plot scale erosion rates up the catchment scale can be problematic (De Vente and Poesen, 2005, Parsons et al., 2006a) since bank erosion (Small et al., 2003) and mass movements (Evans and Warburton, 2007, Evans et al., 2006) form an important part of the catchment sediment budget in upland peat catchments. More field monitoring is needed as a basis for scaling erosion rates from one specific area to larger or smaller areas.

Conclusions

The net topographic change for the field sites was –14 to +30 mm yr^{-1}. Headward migration of the gully head was not active due to the dense vegetation cover on the upper hillslopes. The lateral-bank headcut had the most significant negative topographic changes since flowpaths were concentrated and well connected. Needle-ice formation on the peat surface resulted in a significant expansion of the upper peat layer; while drying and cracking of the peat surface led to a corresponding surface lowering. The main topographic change was observed between surveys that occurred only a few weeks apart when intense rainfall, flow wash, needle ice production or surface desiccation occurred. Thus we advocate that repeated SfM surveys that capture change between events or seasons will be beneficial and cost effective for understanding longer-term peat erosion dynamics. SfM can provide high spatial resolution data to understand long term erosion and processes at event timescales.

Aspect, slope and surface roughness are significant predictors of topographic change at field plot scale. Slope, curvature and roughness are significantly correlated with topographic change at laboratory macroscale.

On the laboratory peat blocks a mean peat loss rate of 0.1 mm (SD: 0.1 mm) was measured by the sediment flux method, compared with a mean peat deposition rate of 0.7 mm (SD: 4.3 mm) derived from the SfM methodology. Hence we have shown that microscale processes are important in producing variable topographic change patterns during sheet wash that can be captured well by SfM methods.

Acknowledgements

The work was jointly funded by the China Scholarship Council and the University of Leeds (File No. 201406040068). Jonathan Carrivick and Lee Brown are thanked for providing the Geodimeter and tinytag temperature loggers used in this study. Special acknowledgement is given to David Ashley who helped prepare the laboratory experimental materials and field set-up. Santiago Clerici and Sarah Hunt are gratefully acknowledged for their time and assistance involved in field work. Duncan Quincey, Scott Watson and Joe Mallalieu are thanked for providing advice on using Agisoft Photoscan and CloudCompare to undertake data analysis. We are grateful to Claudio Bravo L. and Yi-Min Chang Chien (University of Leeds) for providing help in data visualization.

References

ANDERSON, P. 1986. Accidental moorland fires in the Peak District: a study of their incidence and ecological implications. Report to the Peak District Moorland Restoration Project Peak District Planning Board, 164.

BARNHART, T. B. & CROSBY, B. T. 2013. Comparing two methods of surface change detection on an evolving thermokarst using high-temporal-frequency terrestrial laser scanning, Selawik River, Alaska. Remote Sensing, 5, 2813-2837.

BONN, A., ALLOTT, T., EVANS, M., JOOSTEN, H. & STONEMAN, R. 2016. Peatland restoration and ecosystem services: science, policy and practice, Cambridge University Press.

BORRELLI, P., ROBINSON, D. A., FLEISCHER, L. R., LUGATO, E., BALLABIO, C., ALEWELL, C., MEUSBURGER, K., MODUGNO, S., SCHÜTT, B. & FERRO, V. 2017. An assessment of the global impact of 21st century land use change on soil erosion. Nature Communications, 8, 2013.

BOWER, M. 1960a. The erosion of blanket peat in the southern Pennines. East Midland Geographer, 13, 22-33.

BOWER, M. 1960b. Peat erosion in the Pennines. Advancement of Science, 64, 323-331.

BOWER, M. 1961. The distribution of erosion in blanket peat bogs in the Pennines. Transactions and Papers (Institute of British Geographers), 29, 17-30.

BOWYER-BOWER, T. & BURT, T. 1989. Rainfall simulators for investigating soil response to rainfall. Soil Technology, 2, 1-16.

BURT, T. & GARDINER, A. 1984. Runoff and sediment production in a small peat-covered catchment: some preliminary results. Catchment Experiments in Fluvial Geomorphology Norwich, England: Geo Books.

DE VENTE, J. & POESEN, J. 2005. Predicting soil erosion and sediment yield at the basin scale: Scale issues and semi-quantitative models. Earth-Science Reviews, 71, 95-125.

ELTNER, A., KAISER, A., ABELLAN, A. & SCHINDEWOLF, M. 2017. Time lapse structure from motion photogrammetry for continuous geomorphic monitoring. Earth Surface Processes and Landforms, 42, 2240-2253.

EVANS, M., ALLOTT, T., HOLDEN, J., FLITCROFT, C. & BONN, A. 2005. Understanding gully blocking in deep peat. Moors for the Future Report. Derbyshire.

EVANS, M., BURT, T., HOLDEN, J. & ADAMSON, J. 1999. Runoff generation and water table fluctuations in blanket peat: evidence from UK data spanning the dry summer of 1995. Journal of Hydrology, 221, 141-160.

EVANS, M. & LINDSAY, J. 2010a. High resolution quantification of gully erosion in upland peatlands at the landscape scale. Earth Surface Processes and Landforms, 35, 876-886.

EVANS, M. & LINDSAY, J. 2010b. Impact of gully erosion on carbon sequestration in blanket peatlands. Climate Research, 45, 31-41.

EVANS, M. & WARBURTON, J. 2005. Sediment budget for an eroding peat ‐ moorland catchment in northern England. Earth Surface Processes and Landforms, 30, 557-577.

EVANS, M. & WARBURTON, J. 2007. Geomorphology of upland peat: erosion, form and landscape change, Oxford, UK, John Wiley & Sons.

EVANS, M., WARBURTON, J. & YANG, J. 2006. Eroding blanket peat catchments: global and local implications of upland organic sediment budgets. Geomorphology, 79, 45-57.

FONSTAD, M. A., DIETRICH, J. T., COURVILLE, B. C., JENSEN, J. L. & CARBONNEAU, P. E. 2013. Topographic structure from motion: a new development in photogrammetric measurement. Earth Surface Processes and Landforms, 38, 421-430.

FOX, D. M. & BRYAN, R. B. 2000. The relationship of soil loss by interrill erosion to slope gradient. Catena, 38, 211-222.

FRANCIS, I. 1990. Blanket peat erosion in a mid‐wales catchment during two drought years. Earth Surface Processes and Landforms, 15, 445-456.

GLENDELL, M., MCSHANE, G., FARROW, L., JAMES, M. R., QUINTON, J., ANDERSON, K., EVANS, M., BENAUD, P., RAWLINS, B. & MORGAN, D. 2017. Testing the utility of structure‐from‐motion photogrammetry reconstructions using small unmanned aerial vehicles and ground photography to estimate the extent of upland soil erosion. Earth Surface Processes and Landforms, 42, 1860-1871.

GÓMEZ-GUTIÉRREZ, Á., DE SANJOSÉ-BLASCO, J. J., LOZANO-PARRA, J., BERENGUER-SEMPERE, F. & DE MATÍAS-BEJARANO, J. 2015. Does HDR pre-processing improve the accuracy of 3D models obtained by means of two conventional SfM-MVS software packages? The case of the Corral del Veleta Rock Glacier. Remote Sensing, 7, 10269-10294.

GRAYSON, R., HOLDEN, J., JONES, R., CARLE, J. & LLOYD, A. 2012. Improving particulate carbon loss estimates in eroding peatlands through the use of terrestrial laser scanning. Geomorphology, 179, 240-248.

HOLDEN, J. & BURT, T. 2002a. Infiltration, runoff and sediment production in blanket peat catchments: implications of field rainfall simulation experiments. Hydrological Processes, 16, 2537-2557.

HOLDEN, J. & BURT, T. 2002b. Laboratory experiments on drought and runoff in blanket peat. European Journal of Soil Science, 53, 675-690.

HOLDEN, J. & BURT, T. 2003. Hydrological studies on blanket peat: the significance of the acrotelm‐catotelm model. Journal of Ecology, 91, 86-102.

HOLDEN, J., KIRKBY, M. J., LANE, S. N., MILLEDGE, D. G., BROOKES, C. J., HOLDEN, V. & MCDONALD, A. T. 2008. Overland flow velocity and roughness properties in peatlands. Water Resources Research, 44, W06415.

IMESON, A. 1974. The origin of sediment in a moorland catchment with particular reference to the role of vegetation. Institute of British Geographers Special Publication, 6, 59-72.

ISERLOH, T., RIES, J., ARNÁEZ, J., BOIX-FAYOS, C., BUTZEN, V., CERDÀ, A., ECHEVERRÍA, M., FERNÁNDEZ-GÁLVEZ, J., FISTER, W. & GEIßLER, C. 2013. European small portable rainfall simulators: A comparison of rainfall characteristics. Catena, 110, 100-112.

JAMES, M. & ROBSON, S. 2012. Straightforward reconstruction of 3D surfaces and topography with a camera: Accuracy and geoscience application. Journal of Geophysical Research: Earth Surface, 117, F03017.

KAISER, A., NEUGIRG, F., ROCK, G., MÜLLER, C., HAAS, F., RIES, J. & SCHMIDT, J. 2014. Small-scale surface reconstruction and volume calculation of soil erosion in complex Moroccan gully morphology using structure from motion. Remote Sensing, 6, 7050-7080.

KLØVE, B. 1998. Erosion and sediment delivery from peat mines. Soil and Tillage Research, 45, 199-216.

LABADZ, J., BURT, T. & POTTER, A. 1991. Sediment yield and delivery in the blanket peat moorlands of the Southern Pennines. Earth Surface Processes and Landforms, 16, 255-271.

LAGUE, D., BRODU, N. & LEROUX, J. 2013. Accurate 3D comparison of complex topography with terrestrial laser scanner: Application to the Rangitikei canyon (NZ). ISPRS Journal of Photogrammetry and Remote Sensing, 82, 10-26.
LI, C., GRAYSON, R., HOLDEN, J. & LI, P. 2018a. Erosion in peatlands: Recent research progress and future directions. Earth-Science Reviews, 185, 870-886.
LI, C., HOLDEN, J. & GRAYSON, R. 2018b. Effects of needle ice production and thaw on peat erosion processes during overland flow events. Journal of Geophysical Research: Earth Surface, 123, 2107-2122
LI, C., HOLDEN, J. & GRAYSON, R. 2018c. Effects of rainfall, overland flow and their interactions on peatland interrill erosion processes. Earth Surface Processes and Landforms, 43, 1451-1464.
LI, P., HOLDEN, J. & IRVINE, B. 2016a. Prediction of blanket peat erosion across Great Britain under environmental change. Climatic Change, 134, 177-191.
LI, P., HOLDEN, J., IRVINE, B. & GRAYSON, R. 2016b. PESERA - PEAT: a fluvial erosion model for blanket peatlands. Earth Surface Processes and Landforms, 41, 2058-2077.
LI, P., HOLDEN, J., IRVINE, B. & MU, X. 2017. Erosion of Northern Hemisphere blanket peatlands under 21st - century climate change. Geophysical Research Letters, 44, 3615-3623.
MALLALIEU, J., CARRIVICK, J. L., QUINCEY, D. J., SMITH, M. W. & JAMES, W. H. 2017. An integrated Structure-from-Motion and time-lapse technique for quantifying ice-margin dynamics. Journal of Glaciology, 1-13.
MARTÍNEZ-MURILLO, J., NADAL-ROMERO, E., REGÜÉS, D., CERDÀ, A. & POESEN, J. 2013. Soil erosion and hydrology of the western Mediterranean badlands throughout rainfall simulation experiments: a review. Catena, 106, 101-112.
METOFFICE 2018. Maps of climate variables for months, seasons and years https://www.metoffice.gov.uk/climate/uk/summaries/anomacts.
MICHELETTI, N., CHANDLER, J. H. & LANE, S. N. 2015a. Investigating the geomorphological potential of freely available and accessible structure - from - motion photogrammetry using a smartphone. Earth Surface Processes and Landforms, 40, 473-486.
MICHELETTI, N., CHANDLER, J. H. & LANE, S. N. 2015b. Structure from motion (SFM) photogrammetry. In: CLARKE, L. E. & NIELD, J. M. (eds.) Geomorphological Techniques (Online Edition). London: British Society for Geomorphology.
MORGAN, J. A., BROGAN, D. J. & NELSON, P. A. 2017. Application of Structure-from-Motion photogrammetry in laboratory flumes. Geomorphology, 276, 125-143.
MOSELY, M. 1972. Gully systems in blanket peat, Bleaklow, North Derbyshire. East Midland Geographer, 5, 235-244.
NATIONALRIVERFLOWARCHIVE 2018. Catchment daily rainfall record of Snaizeholme Beck at Low Houses (1961-2015) https://nrfa.ceh.ac.uk/data/station/meanflow/27047.
PARSONS, A. J., BRAZIER, R. E., WAINWRIGHT, J. & POWELL, D. M. 2006a. Scale relationships in hillslope runoff and erosion. Earth Surface Processes and Landforms, 31, 1384-1393.
PARSONS, A. J., WAINWRIGHT, J., BRAZIER, R. E. & POWELL, D. M. 2006b. Is sediment delivery a fallacy? Earth Surface Processes and Landforms, 31, 1325-1328.
PROSDOCIMI, M., BURGUET, M., DI PRIMA, S., SOFIA, G., TEROL, E., COMINO, J. R., CERDÀ, A. & TAROLLI, P. 2017. Rainfall simulation and Structure-from-Motion photogrammetry for the analysis of soil water erosion in Mediterranean vineyards. Science of the Total Environment, 574, 204-215.

ROTHWELL, J. J., LINDSAY, J. B., EVANS, M. G. & ALLOTT, T. E. 2010. Modelling suspended sediment lead concentrations in contaminated peatland catchments using digital terrain analysis. Ecological Engineering, 36, 623-630.

SMALL, I., ROWAN, J. & DUCK, R. 2003. Long-term sediment yield in Crombie Reservoir catchment, Angus; and its regional significance within the Midland Valley of Scotland. Hydrological Sciences Journal, 48, 619-635.

SMITH, M., CARRIVICK, J., HOOKE, J. & KIRKBY, M. 2014. Reconstructing flash flood magnitudes using 'Structure-from-Motion': A rapid assessment tool. Journal of Hydrology, 519, 1914-1927.

SMITH, M., CARRIVICK, J. & QUINCEY, D. 2016. Structure from motion photogrammetry in physical geography. Progress in Physical Geography, 40, 247-275.

SMITH, M. & WARBURTON, J. 2018. Microtopography of bare peat: a conceptual model and objective classification from high‐resolution topographic survey data. Earth Surface Processes and Landforms, 43, 1557-1574.

SMITH, M. W. & VERICAT, D. 2015. From experimental plots to experimental landscapes: topography, erosion and deposition in sub‐humid badlands from structure‐from‐motion photogrammetry. Earth Surface Processes and Landforms, 40, 1656-1671.

SNAPIR, B., HOBBS, S. & WAINE, T. 2014. Roughness measurements over an agricultural soil surface with Structure from Motion. ISPRS Journal of Photogrammetry and Remote Sensing, 96, 210-223.

STÖCKER, C., ELTNER, A. & KARRASCH, P. 2015. Measuring gullies by synergetic application of UAV and close range photogrammetry—A case study from Andalusia, Spain. Catena, 132, 1-11.

STUMPF, A., MALET, J.-P., ALLEMAND, P., PIERROT-DESEILLIGNY, M. & SKUPINSKI, G. 2015. Ground-based multi-view photogrammetry for the monitoring of landslide deformation and erosion. Geomorphology, 231, 130-145.

TALLIS, J. & YALDEN, D. 1983. Peak District Moorland Restoration Project Phase 2 Report. Peak District National Park Authority, Bakewell.

TUUKKANEN, T., STENBERG, L., MARTTILA, H., FINÉR, L., PIIRAINEN, S., KOIVUSALO, H. & KLØVE, B. 2016. Erosion mechanisms and sediment sources in a peatland forest after ditch cleaning. Earth Surface Processes and Landforms, 41, 1841-1853.

VERICAT, D., SMITH, M. & BRASINGTON, J. 2014. Patterns of topographic change in sub-humid badlands determined by high resolution multi-temporal topographic surveys. Catena, 120, 164-176.

WATSON, C. S., QUINCEY, D. J., SMITH, M. W., CARRIVICK, J. L., ROWAN, A. V. & JAMES, M. R. 2017. Quantifying ice cliff evolution with multi-temporal point clouds on the debris-covered Khumbu Glacier, Nepal. Journal of Glaciology, 63, 823-837.

WESTOBY, M. J., DUNNING, S. A., HEIN, A. S., MARRERO, S. M. & SUGDEN, D. E. 2016. Interannual surface evolution of an Antarctic blue-ice moraine using multi-temporal DEMs. Earth Surface Dynamics, 4, 515.

WHEATON, J. M., BRASINGTON, J., DARBY, S. E., KASPRAK, A., SEAR, D. & VERICAT, D. 2013. Morphodynamic signatures of braiding mechanisms as expressed through change in sediment storage in a gravel‐bed river. Journal of Geophysical Research: Earth Surface, 118, 759-779.

XU, J., MORRIS, P. J., LIU, J. & HOLDEN, J. 2018. PEATMAP: Refining estimates of global peatland distribution based on a meta-analysis. Catena, 160, 134-140.

YU, Z. 2012. Northern peatland carbon stocks and dynamics: a review. Biogeosciences, 9, 4071-4085.

Tables

Table 1. Summary of georeferencing errors (i.e. RMSE on control points) for the field surveys. The Six GCPs were used to reconstruct dense points for the field models. Notes refer to weather conditions on the date of survey.

Site	Survey date	No.	No. of images	Georeferencing RMSE (mm)	Notes
Site 1	26/10/2016	1	69	52.4	
	04/11/2016	2	97	53.4	
	30/11/2016	3	79	50.7	Freezing/Needle-ice
	21/12/2016	4	101	56.9	Slightly misty/ Needle-ice
	22/02/2017	5	93	56.6	Needle-ice thaw
	07/04/2017	6	88	44.4	Slight desiccation
	02/05/2017	7	74	47.4	Serious desiccation
	13/06/2017	8	79	46.8	
	21/08/2017	9	50	41.6	
	27/09/2017	10	112	59.3	
	02/11/2017	11	48	54.3	
Site 2	26/10/2016	1	47	16.5	
	04/11/2016	2	137	17.7	
	30/11/2016	3	60	23.6	Needle-ice formation
	21/12/2016	4	85	25.0	Needle-ice thawing/ misty
	22/02/2017	5	101	21.3	Needle-ice thaw
	07/04/2017	6	123	18.4	Slight desiccation
	02/05/2017	7	136	20.7	Serious desiccation
	13/06/2017	8	134	15.9	
	21/08/2017	9	107	18.8	

Site	Survey date	No.	No. of images	Georeferencing RMSE (mm)	Notes
	27/09/2017	10	114	17.4	
	02/11/2017	11	41	18.6	
	26/10/2016	1	23	39.7	
	04/11/2016	2	68	41.6	
	30/11/2016	3	80	39.1	Freezing/Needle-ice
	21/12/2016	4	114	41.7	Misty
	22/02/2017	5	94	41.1	Needle-ice thaw
Site 3	07/04/2017	6	54	40.5	Slight desiccation
	02/05/2017	7	102	40.7	Serious desiccation
	13/06/2017	8	64	45.5	
	21/08/2017	9	73	41.9	
	27/09/2017	10	76	43.3	
	02/11/2017	11	35	38.3	
	26/10/2016	1	53	39.1	
	04/11/2016	2	52	23.1	
	22/02/2017	3	110	16.3	Needle-ice thaw
	07/04/2017	4	156	16.6	Slight desiccation
Site 4	02/05/2017	5	131	14.8	Serious desiccation
	13/06/2017	6	134	19.6	
	21/08/2017	7	90	16.1	
	27/09/2017	8	79	17.2	
	02/11/2017	9	41	16.9	

Table 2. Summary of the laboratory experimental design and treatments.

Slope	Treatment	Replicate	Total Water Supply (mm hr^{-1})	Rainfall Intensity (mm hr^{-1})	Upslope Inflow Rate (mm hr^{-1})	Duration (min)
2.5°	Rainfall	1	12	12	0	120
		2	12	12	0	120
	Inflow	1	12	0	12	120
		2	12	0	12	120
	Rainfall + Inflow	1	24	12	12	120
		2	24	12	12	120
7.5°	Rainfall	1	12	12	0	120
		2	12	12	0	120
	Inflow	1	12	0	12	120
		2	12	0	12	120
	Rainfall + Inflow	1	24	12	12	120
		2	24	12	12	120

Table 3. Summary of georeferencing errors (i.e. RMSE on control points) for the laboratory surveys.

Survey	No. of images	No. of GCPs	Georeferencing RMSE (mm)
Rainfall[a] (2.5°) [b]_test 1[c]_pre[d]	38	23	4.5
Rainfall (2.5°)_test 1_post	54	23	4.5
Rainfall (2.5°)_test 2_pre	63	23	4.6
Rainfall (2.5°)_test 2_post	73	23	4.7
Inflow (2.5°)_test 1_pre	57	23	4.5
Inflow (2.5°)_test 1_post	63	23	4.6
Inflow (2.5°)_test 2_pre	48	23	4.2
Inflow (2.5°)_test 2_post	51	23	4.6
Rainfall + Inflow (2.5°)_test 1_pre	51	23	5.1
Rainfall + Inflow (2.5°)_test 1_post	48	23	4.2
Rainfall + Inflow (2.5°)_test 2_pre	54	23	4.5
Rainfall + Inflow (2.5°)_test 2_post	61	23	4.6
Rainfall (7.5°)_test 1_pre	33	23	4.2
Rainfall (7.5°)_test 1_post	52	23	4.6
Rainfall (7.5°)_test 2_pre	43	23	4.4
Rainfall (7.5°)_test 2_post	52	23	4.6
Inflow (7.5°)_test 1_pre	33	23	4.5
Inflow (7.5°)_test 1_post	43	23	4.4
Inflow (7.5°)_test 2_pre	34	23	5.6
Inflow (7.5°)_test 2_post	48	23	4.6
Rainfall + Inflow (7.5°)_test 1_pre	39	23	4.5
Rainfall + Inflow (7.5°)_test 1_post	34	23	5.6
Rainfall + Inflow (7.5°)_test 2_pre	52	23	4.6
Rainfall + Inflow (7.5°)_test 2_post	43	23	5.3

a: three types of laboratory experiments include Rainfall events, Inflow events and Rainfall + Inflow events;
b: two slope gradients include 2.5° and 7.5°;
c: two replicates for each type of simulation experiments include test 1 and test 2;
d: two surveys for each test include survey before and after the laboratory simulation tests.

Table 4. Median net, positive and negative topographic changes (mm) with root mean square (RMS) (mm) over different survey intervals for each field site. The long-term survey intervals are highlighted with bold.

Sites	Model*	Differencing period	Net change		Positive change		Negative change	
			Median	RMS**	Median	RMS	Median	RMS
Site 1	2–1	26/10/2016–04/11/2016	–16	24	14	16	–18	25
	3–2	04/11/2016–30/11/2016	14	19	15	18	–17	24
	4–3	30/11/2016–21/12/2016	23	37	23	37	–11	12
	5–4	21/12/2016–22/02/2017	10	15	13	15	–13	15
	6–5	22/02/2017–07/04/2017	–30	42	13	14	–40	45
	7–6	07/04/2017–02/05/2017	12	16	14	17	–13	15
	8–7	02/05/2017–13/06/2017	–14	19	14	16	–16	19
	9–8	13/06/2017–21/08/2017	–10	17	15	18	–14	16
	10–9	21/08/2017–27/09/2017	32	33	36	36	–17	20
	11–10	27/09/2017–02/11/2017	–11	16	16	19	–13	15
	11–1	**26/10/2016–02/11/2017**	**–14**	**19**	**15**	**20**	**–16**	**19**
Site 2	2–1	26/10/2016–04/11/2016	–15	22	16	19	–19	23
	3–2	04/11/2016–30/11/2016	18	21	18	21	–14	16
	4–3	30/11/2016–21/12/2016	–13	18	18	22	–15	16
	5–4	21/12/2016–22/02/2017	12	17	14	16	–15	17
	6–5	22/02/2017–07/04/2017	–14	19	16	21	–17	18
	7–6	07/04/2017–02/05/2017	–12	18	13	14	–15	20
	8–7	02/05/2017–13/06/2017	–15	18	14	17	–16	19
	9–8	13/06/2017–21/08/2017	10	17	14	18	–13	15
	10–9	21/08/2017–27/09/2017	–12	15	13	15	–13	15
	11–10	27/09/2017–02/11/2017	14	20	16	20	–14	19
	11–1	**26/10/2016–02/11/2017**	**–13**	**23**	**18**	**21**	**–19**	**24**
Site 3	2–1	26/10/2016–04/11/2016	–12	14	11	11	–12	14
	3–2	04/11/2016–30/11/2016	17	18	17	18	–19	26

Sites	Model*	Differencing period	Net change		Positive change		Negative change	
			Median	RMS**	Median	RMS	Median	RMS
	4–3	30/11/2016–21/12/2016	–14	17	13	18	–15	16
	5–4	21/12/2016–22/02/2017	11	13	12	14	–12	12
	6–5	22/02/2017–07/04/2017	–11	12	–	–	–11	12
	7–6	07/04/2017–02/05/2017	11	12	12	12	–11	11
	8–7	02/05/2017–13/06/2017	–14	17	12	14	–15	17
	9–8	13/06/2017–21/08/2017	12	16	15	18	–12	12
	10–9	21/08/2017–27/09/2017	–14	16	12	13	–15	16
	11–10	27/09/2017–02/11/2017	30	40	30	40	–	–
	11–1	**26/10/2016–02/11/2017**	**30**	**35**	**32**	**36**	**–14**	**15**
	2–1	26/10/2016–04/11/2016	26	34	26	34	–12	14
	3–2	04/11/2016–22/02/2017	10	21	19	25	–14	17
	4–3	22/02/2017–07/04/2017	–12	17	13	16	–14	18
	5–4	07/04/2017–02/05/2017	11	14	12	13	–14	16
Site 4	6–5	02/05/2017–13/06/2017	13	21	16	22	–14	17
	7–6	13/06/2017–21/08/2017	–18	23	16	19	–19	23
	8–7	21/08/2017–27/09/2017	15	21	18	22	–13	16
	9–8	27/09/2017–26/10/2016	–16	24	14	25	–19	24
	9–1	**26/10/2016–02/11/2017**	**22**	**29**	**25**	**29**	**–22**	**25**

Note: * Model shows comparisons over different survey intervals; ** RMS is the square root of the arithmetic mean of the squares of the set of values.

Table 5. Spearman's rank correlation coefficients between topographic variables and observed topographic change. Significant correlations ($p < 0.05$) are indicated with an asterisk while the strongest relationship for each survey period is also highlighted in bold.

Sites	Model		Aspect	Slope	Curvature	Profile curvature	Plan curvature	Roughness
	2–1	Total	**0.185***	–0.000	0.015*	–0.014*	0.014*	0.037*
		Positive	0.041*	–0.006	0.018*	–0.013	0.018*	**0.304***
		Negative	0.126*	–0.007	0.012*	–0.011*	0.011*	**–0.170***
	3–2	Total	0.090*	**–0.104***	0.026*	–0.027*	0.015*	–0.000
		Positive	0.062*	–0.094*	0.015*	–0.018*	0.009*	**0.194***
		Negative	0.061*	–0.151*	0.012	–0.018*	–0.014	**–0.285***
	4–3	Total	–0.127*	0.208*	0.008*	–0.007	0.005	**0.555***
		Positive	–0.128*	0.223*	0.004	–0.003	0.002	**0.529***
		Negative	**–0.234***	–0.045*	0.056*	–0.063*	0.025	–0.085*
	5–4	Total	**0.293***	–0.114*	0.020*	–0.032*	0.003	0.121*
		Positive	0.109*	0.065*	0.016	–0.022*	0.004	**0.134***
Site 1		Negative	–0.007	0.011	0.019*	–0.027*	0.005	**–0.048***
	6–5	Total	**0.139***	0.065*	0.010*	–0.008*	0.009*	0.000
		Positive	0.026*	**0.040***	0.003	–0.008	–0.004	0.007
		Negative	**0.176***	–0.037*	0.000	0.000	–0.001	0.073*
	7–6	Total	0.150*	**–0.169***	0.047*	–0.048*	0.028*	0.131*
		Positive	0.087*	0.096*	0.013*	–0.012*	0.008	**0.151***
		Negative	–0.022*	**–0.224***	0.016	–0.028*	–0.011	–0.124*
	8–7	Total	–0.042*	0.030*	0.053*	–0.040*	0.054*	**–0.178***
		Positive	–0.008	**0.053***	0.014	–0.014	0.008	–0.015
		Negative	0.015*	–0.119*	0.029*	–0.024*	0.027*	**–0.135***
	9–8	Total	–0.012*	–0.033*	0.053*	–0.052*	0.034*	**0.078***
		Positive	–0.103*	**0.123***	0.012	–0.013*	0.006	0.060*

Sites	Model		Aspect	Slope	Curvature	Profile curvature	Plan curvature	Roughness
		Negative	–0.012*	**–0.109***	0.027*	–0.023*	0.020*	–0.058*
	10–9	Total	–0.136*	**–0.211***	0.014*	–0.017*	0.006*	0.028*
		Positive	**–0.180***	0.037*	0.013*	–0.008*	0.017*	–0.145*
		Negative	–0.047*	**0.055***	0.019*	–0.021*	0.009	–0.034*
	11–10	Total	**–0.341***	0.210*	0.056*	–0.039*	0.062*	0.062*
		Positive	–0.158*	0.230*	0.026*	–0.029*	0.013	**0.255***
		Negative	–0.202*	**–0.221***	0.032*	–0.020*	0.039*	–0.205*
	11–1	Total	–0.017*	–0.024*	0.052*	–0.055*	0.036*	**0.280***
		Positive	–0.001	0.144*	0.015	–0.016	0.012	**0.315***
		Negative	**–0.078***	–0.067*	0.039*	–0.043*	0.022*	0.040*
Site 2	2–1	Total	–0.013*	**–0.070***	0.036*	–0.038*	0.018*	–0.067*
		Positive	0.051*	**0.099***	0.014*	–0.015*	0.004	0.071*
		Negative	0.043*	–0.156*	0.027*	–0.028*	0.014*	**–0.239***
	3–2	Total	–0.094*	0.123*	0.006*	–0.006*	0.005*	**0.297***
		Positive	–0.103*	0.138*	0.005*	–0.006*	0.003	**0.334***
		Negative	0.110*	–0.176*	0.006	–0.003	0.009	**–0.246***
	4–3	Total	–0.052*	–0.017*	0.004	0.006*	0.025*	**0.254***
		Positive	–0.105*	0.094*	0.002	0.002	0.014*	**0.151***
		Negative	0.030*	**–0.089***	0.017*	–0.014*	0.018*	0.000
	5–4	Total	–0.008*	0.118*	0.021*	–0.024*	0.010*	**0.126***
		Positive	–0.083*	0.050*	0.008*	–0.009*	0.004	**0.124***
		Negative	0.066*	0.002	0.015*	–0.020*	0.001	**–0.163***
	6–5	Total	–0.032*	0.139*	–0.004	0.004	0.002	**0.161***
		Positive	–0.132*	–0.017*	–0.008*	0.008*	–0.003	**0.246***
		Negative	**–0.063***	–0.047*	0.004	–0.005	0.002	0.035*
	7–6	Total	0.078*	**–0.159***	0.071*	–0.077*	0.030*	–0.141*
		Positive	0.040*	0.090*	0.008	–0.009	0.002	**0.168***
		Negative	**0.142***	–0.101*	0.060*	–0.067*	0.024*	–0.073*

Sites	Model		Aspect	Slope	Curvature	Profile curvature	Plan curvature	Roughness
	8–7	Total	0.007*	–0.061*	0.011*	–0.010*	0.014*	**0.121***
		Positive	–0.071*	0.065*	0.012	–0.022*	0.002	**0.123***
		Negative	–0.022*	**–0.143***	0.006	–0.004	0.008*	0.042*
	9–8	Total	–0.047*	–0.056*	0.068*	**–0.073***	0.040*	–0.030*
		Positive	–0.057*	0.065*	0.044*	–0.039*	0.043*	**0.101***
		Negative	0.029*	–0.100*	0.032*	–0.038*	0.011*	**–0.169***
	10–9	Total	0.042*	**0.128***	0.027*	–0.027*	0.023*	0.059*
		Positive	–0.060*	0.120*	0.046*	–0.038*	0.045*	**0.308***
		Negative	0.104*	–0.048*	0.017*	–0.019*	0.008	**–0.271***
	11–10	Total	–0.038*	–0.048*	0.014*	–0.012*	0.009*	**0.102***
		Positive	–0.084*	**0.097***	0.008	–0.008	0.006	0.005
		Negative	0.067*	–0.016*	0.009	–0.011	0.001	**–0.105***
	11–1	Total	–0.030*	0.097*	0.027*	–0.027*	0.016*	**0.109***
		Positive	–0.033*	0.091*	0.008	–0.005	0.007	**0.177***
		Negative	–0.030*	–0.076*	0.019*	–0.018*	0.012*	**–0.129***
Site 3	2–1	Total	–0.068*	–0.004	0.000	0.004	0.005	**0.171***
		Positive	0.052	**0.245***	0.024	–0.007	0.074	0.227*
		Negative	–0.026*	**–0.231***	–0.004	0.014	0.008	–0.159*
	3–2	Total	**–0.161***	–0.029*	0.002	0.007*	0.011*	0.102*
		Positive	**–0.157***	–0.061*	–0.002	0.009*	0.007*	0.053*
		Negative	0.275*	–0.283*	0.007	0.001	0.021	**–0.460***
	4–3	Total	0.057*	**0.071***	0.029*	–0.051*	–0.001	0.024*
		Positive	–0.063*	0.159*	0.050*	–0.056*	0.040*	**0.376***
		Negative	0.023*	–0.006	0.023*	–0.030*	0.005	**0.103***
	5–4	Total	0.125*	0.207*	0.010	–0.013	0.004	**0.430***
		Positive	0.007	0.296*	0.013	–0.018	0.004	**0.410***
		Negative	0.061*	**–0.067***	0.036*	–0.029*	0.035*	–0.024*
	6–5	Total	**–0.104***	–0.032*	0.005	–0.007	0.002	–0.065*

Sites	Model		Aspect	Slope	Curvature	Profile curvature	Plan curvature	Roughness
		Positive	–	–	–	–	–	–
		Negative	**–0.065***	–0.025*	0.001	–0.002	0.002	–0.033*
	7–6	Total	0.200*	0.079*	0.050	–0.063*	0.025	**0.362***
		Positive	0.040	0.219*	0.043	–0.066	0.010	**0.326***
		Negative	0.052	–0.321*	0.007	0.025	0.011	**–0.341***
	8–7	Total	0.040*	–0.136*	0.033*	–0.029*	0.030*	**–0.170***
		Positive	–0.092*	0.182*	0.026*	–0.023*	0.022	**0.201***
		Negative	–0.094*	–0.193*	0.023*	–0.022*	0.016*	**–0.203***
	9–8	Total	0.159*	0.352*	0.028*	–0.041*	0.009	**0.464***
		Positive	–0.045*	0.187*	0.034*	–0.034*	0.019*	**0.432***
		Negative	–0.052*	**–0.183***	0.023	–0.021	0.017	–0.171*
	10–9	Total	**0.111***	–0.011*	0.011*	–0.009*	0.012*	0.079*
		Positive	–0.148*	**0.166***	0.003	–0.004	0.009	0.072*
		Negative	**0.075***	–0.067*	0.008	–0.012*	0.005	–0.036*
	11–10	Total	0.232*	**0.363***	0.007*	–0.013*	–0.001	0.170*
		Positive	0.298*	**0.326***	0.014*	–0.017*	0.005*	0.093*
		Negative	–	–	–	–	–	–
	11–1	Total	0.351*	**0.426***	0.001	–0.008	–0.007	0.050*
		Positive	0.070*	**0.463***	0.011*	–0.013*	0.005*	0.072*
		Negative	0.111*	**–0.433***	–0.053	0.076	–0.022	–0.259*
Site 4	2–1	Total	0.091*	0.028*	–0.002	0.003	0.001	**0.180***
		Positive	0.093*	0.030*	–0.003	0.003	0.001	**0.185***
		Negative	–0.012	–0.209*	0.004	0.012	0.029	**–0.222***
	3–2	Total	0.121*	0.069*	0.045*	–0.046*	0.033*	**0.122***
		Positive	0.089*	**0.200***	0.006	–0.007	0.006	0.060*
		Negative	–0.063*	**–0.155***	0.031*	–0.035*	0.020*	–0.154*
	4–3	Total	–0.025*	**–0.091***	0.030*	–0.031*	0.020*	0.015*
		Positive	0.028*	**0.084***	0.015	–0.014	0.005	0.066*

Sites	Model		Aspect	Slope	Curvature	Profile curvature	Plan curvature	Roughness
		Negative	–0.056*	**–0.212***	0.018*	–0.021*	0.014*	–0.201*
	5–4	Total	0.009	**–0.100***	0.046*	–0.051*	0.025*	0.068*
		Positive	0.066*	**0.131***	0.012	–0.014*	0.006	0.101*
		Negative	0.011	**–0.063***	0.036*	–0.034*	0.023*	–0.059*
	6–5	Total	0.090*	**–0.023***	0.021*	–0.012*	0.031*	0.000
		Positive	0.134*	**0.179***	0.005	0.000	0.010*	0.068*
		Negative	–0.078*	–0.206*	0.032*	–0.030*	0.029*	**–0.276***
	7–6	Total	**–0.108***	–0.010*	0.035*	–0.042*	0.012*	0.046*
		Positive	0.037*	**0.063***	0.024*	–0.023*	0.020*	0.058*
		Negative	**–0.137***	–0.088*	0.029*	–0.035*	0.010*	–0.033*
	8–7	Total	**0.123***	–0.101*	0.015*	–0.014*	0.010*	0.080*
		Positive	**0.155***	–0.003	0.007	–0.007	0.004	0.079*
		Negative	–0.053*	–0.135*	0.007	–0.014	–0.003	**–0.170***
	9–8	Total	**–0.095***	0.010*	0.061*	–0.066*	0.039*	–0.047*
		Positive	0.090*	0.195*	0.061*	–0.048*	0.067*	**0.196***
		Negative	–0.114*	–0.107*	0.042*	–0.052*	0.015*	**–0.172***
	9–1	Total	0.001	0.009*	0.006*	–0.005	0.010*	**0.089***
		Positive	0.015*	0.045*	0.004	–0.002	0.009*	**0.133***
		Negative	**–0.276***	0.024	–0.009	0.004	–0.012	–0.212*

Table 6. Summary of meteorological data for both short-term and long-term monitoring periods. Frost cycles indicate the number of times soil surface temperature fell below 0 ºC and also returned above 0 ºC; both have to occur to count as one cycle.

Scale	Monitoring interval	Number of days (rainy days)	Total rainfall (mm)	Maximum rainfall (mm/15’)	Mean temperature (ºC)	Days, T < ºC	Frost cycles
	26/10/2016–04/11/2016	10 (4)	14.6	0.2	6.4	4	6
	04/11/2016–30/11/2016	27 (19)	103.6	2.2	1.5	7	20
	30/11/2016–21/12/2016	22 (17)	50.6	1.4	4.8	3	3
	21/12/2016–22/02/2017	64 (45)	225.4	2.0	1.7	31	44
Short-term	22/02/2017–07/04/2017	45 (36)	320.8	3.0	4.4	10	6
	07/04/2017–02/05/2017	26 (12)	20.0	0.2	6.1	6	5
	02/05/2017–13/06/2017	43 (26)	225.4	2.2	11.2	1	1
	13/06/2017–21/08/2017	70 (52)	457.0	3.4	13.5	0	0
	21/08/2017–27/09/2017	38 (30)	226.4	7.2	–	–	–
	27/09/2017–02/11/2017	37 (30)	396.4	3.6	–	–	–
Long-term	04/11/2016–22/02/2017	112 (80)	379.6	2.2	2.6	41	66
	26/10/2016–02/11/2017	373 (266)	2012.0	7.2	–	–	–

Table 7. Summary of the median net, positive and negative topographic changes (mm) with root mean square (RMS) (mm) for laboratory models.

Model	Net change		Positive change		Negative change	
	Median	RMS[d]	Median	RMS	Median	RMS
Rainfall[a] (2.5°)[b]_test 1[c]	–5	6	6	9	–5	6
Rainfall (2.5°)_test 2	–4	6	4	5	–5	7
Inflow (2.5°)_test 1	4	8	5	8	–6	7
Inflow (2.5°)_test 2	–3	5	4	5	–5	6
Rainfall + Inflow (2.5°)_test 1	–5	7	5	6	–6	7
Rainfall + Inflow (2.5°)_test 2	4	5	4	5	–4	5
Rainfall (7.5°)_test 1	4	7	5	7	–4	6
Rainfall (7.5°)_test 2	–4	5	4	5	–4	5
Inflow (7.5°)_test 1	3	6	5	6	–5	6
Inflow (7.5°)_test 2	5	6	5	6	–5	7
Rainfall + Inflow (7.5°)_test 1	–4	7	4	5	–5	7
Rainfall + Inflow (7.5°)_test 2	–5	6	5	6	–5	6

a: three types of laboratory experiments include Rainfall events, Inflow events and Rainfall + Inflow events;

b: two slope gradients include 2.5° and 7.5°;

c: two replicates for each type of simulation experiments include test 1 and test 2;

d: RMS is the square root of the arithmetic mean of the squares of the set of values.

Table 8. Spearman's rank correlation coefficients between topographic variables and observed topographic change for the laboratory peat blocks. Significant correlations ($p < 0.05$) are indicated with an asterisk while the strongest relationship for each survey period is also highlighted in bold.

Model		Aspect	Slope	Curvature	Profile curvature	Plan curvature	Roughness
	Total	–0.007	–0.090*	**–0.154***	0.142*	–0.128*	–0.120*
2.5R1	Positive	–0.033	**0.234***	–0.106*	0.104*	–0.072*	–0.152*
	Negative	0.004	**–0.222***	–0.110*	0.104*	–0.089*	–0.073*
	Total	0.003	–0.066*	**–0.131***	0.113*	–0.117*	–0.114*
2.5R2	Positive	–0.101*	**0.308***	–0.097*	0.064*	–0.127*	0.260*
	Negative	0.017	**–0.175***	–0.031*	0.025	–0.026	–0.094*
	Total	–0.025*	0.050*	**–0.132***	0.105*	–0.129*	–0.106*
2.5F1	Positive	0.003	**0.162***	–0.079*	0.048*	–0.096*	–0.125*
	Negative	–0.015	**0.072***	0.033	–0.035	0.011	–0.039*
	Total	–0.079*	–0.072*	**–0.152***	0.149*	–0.120*	–0.033*
2.5F2	Positive	–0.064*	**0.142***	–0.053*	0.051*	–0.059*	–0.058*
	Negative	0.014	**–0.093***	0.002	–0.011	–0.012	–0.010
	Total	0.052*	–0.114*	**–0.116***	0.105*	–0.098*	–0.104*
2.5RF1	Positive	0.053*	**0.217***	–0.037*	0.014	–0.055*	–0.184*
	Negative	0.028*	**–0.221***	–0.055*	0.050*	–0.040*	0.039*
	Total	–0.072*	–0.023*	**–0.184***	0.167*	–0.167*	–0.045*
2.5RF2	Positive	–0.066*	**0.189***	–0.121*	0.108*	–0.110*	–0.005
	Negative	–0.015	**–0.200***	–0.111*	0.094*	–0.109*	0.021
	Total	–0.096*	**0.291***	–0.186*	0.157*	–0.177*	0.077*
7.5R1	Positive	–0.134*	**0.437***	–0.185*	0.150*	–0.185*	0.137*
	Negative	–0.019	–0.140*	0.015	–0.015	0.025	**–0.207***
	Total	–0.013	–0.040*	**–0.082***	0.080*	–0.067*	0.003
7.5R2	Positive	–0.052*	0.086*	–0.058*	0.057*	–0.041*	**0.109***
	Negative	0.032*	–0.122*	–0.034*	0.036*	–0.025*	**–0.165***

Model		Aspect	Slope	Curvature	Profile curvature	Plan curvature	Roughness
7.5F1	Total	0.080*	0.110*	–0.147*	0.136*	–0.119*	**–0.205***
	Positive	–0.064*	**0.174***	–0.102*	0.098*	–0.081*	–0.132*
	Negative	0.038*	–0.043*	–0.036*	0.038*	–0.023	**–0.065***
7.5F2	Total	0.019	0.009	**–0.109***	0.106*	–0.082*	0.002
	Positive	0.013	**0.122***	–0.068*	0.061*	–0.059*	–0.003
	Negative	0.081*	**–0.273***	–0.058	0.045	–0.033	–0.047
7.5RF1	Total	0.074*	0.090*	–0.084*	0.076*	–0.077*	**–0.104***
	Positive	–0.054*	**0.159***	–0.055*	0.044*	–0.057*	0.135*
	Negative	0.056*	–0.045*	–0.049*	0.048*	–0.046*	**–0.140***
7.5RF2	Total	0.038*	0.023*	**–0.052***	0.049*	–0.042*	–0.005*
	Positive	–0.100*	0.080*	–0.062*	0.071*	–0.045	**0.230***
	Negative	0.023*	–0.073*	–0.021*	0.019*	–0.018	**–0.102***

Figures

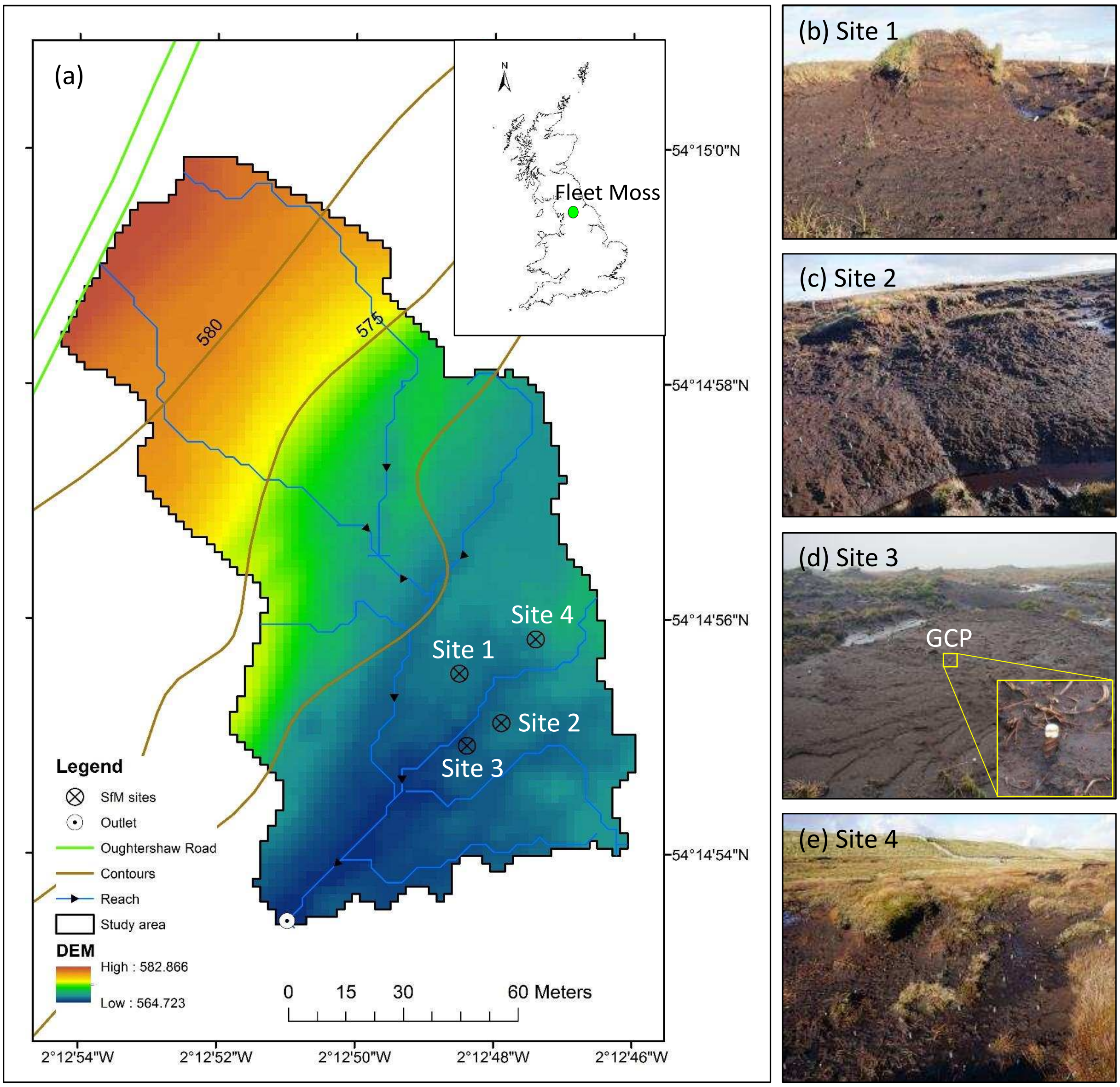

Figure 1. (a) Map showing the location of Fleet Moss and the distribution of SfM surveyed sites with different erosion features. A digital elevation model (DEM) across Fleet Moss was provided based on LiDAR data (2 m ground resolution, 250 mm z resolution); (b) Site 1 (21.3 m^2) is a peat hagg that is severely eroded by wind; (c) Site 2 (25.9 m^2) is a peat gully wall side; (d) Site 3 (27.5 m^2) is a flat hilltoe area adjacent to the stream. One of the GCPs used in the study can also be seen; (e) Site 4 (19.3 m^2) is a gully head.

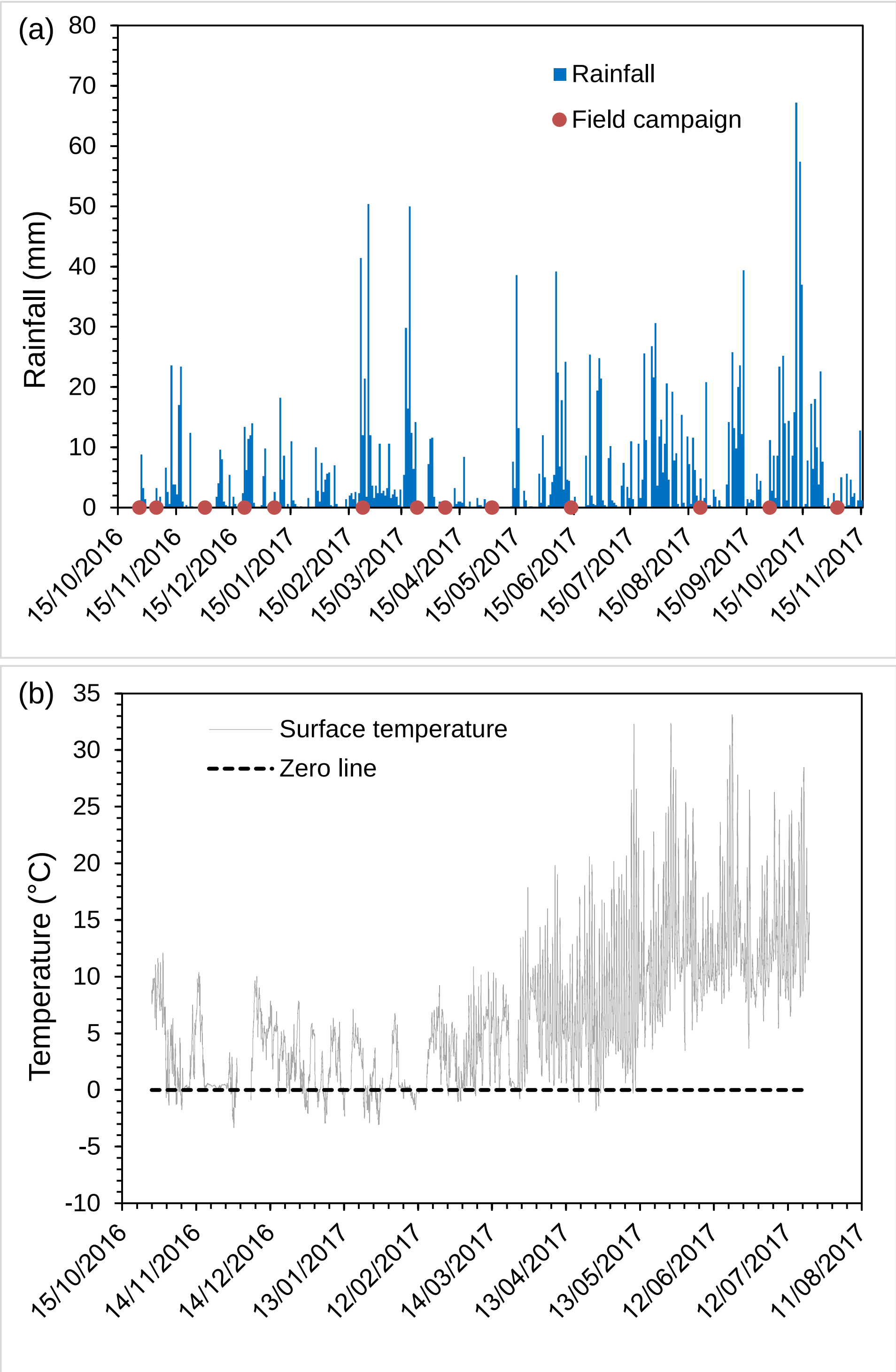

Figure 2. Meteorological data during the intensive survey period including (a) daily total rainfall and (b) peat surface temperature. Time of SfM measurements are indicated with red points in diagram (a). Dashed black line in diagram (b) indicates the freezing threshold (i.e. 0 ℃).

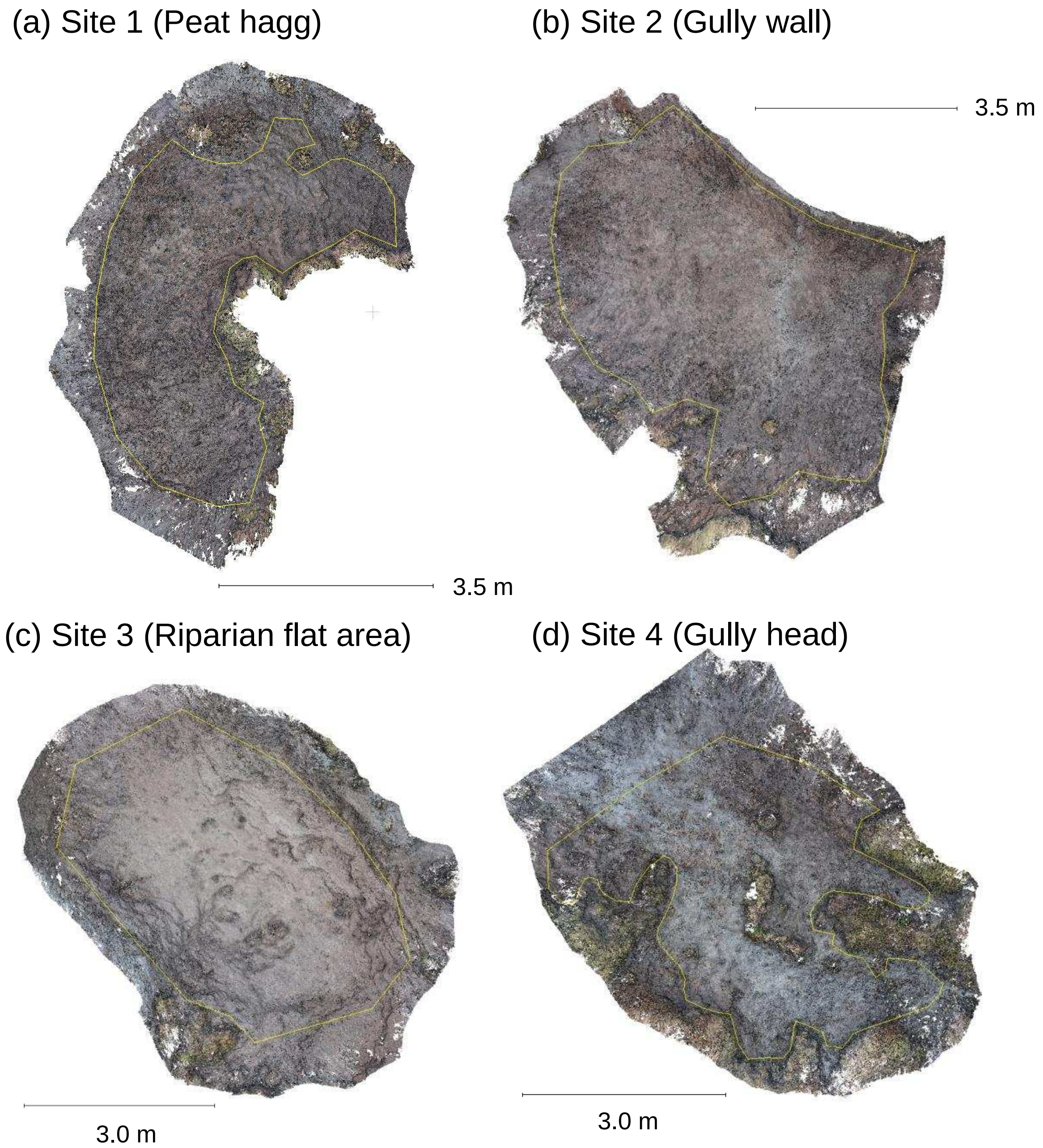

Figure 3. Top view on the features of interest (with boundary marked as yellow): (a) Site 1 (peat hagg); (b) Site 2 (Gully wall); (c) Site 3 (Riparian flat area) and (d) Site 4 (Gully head).

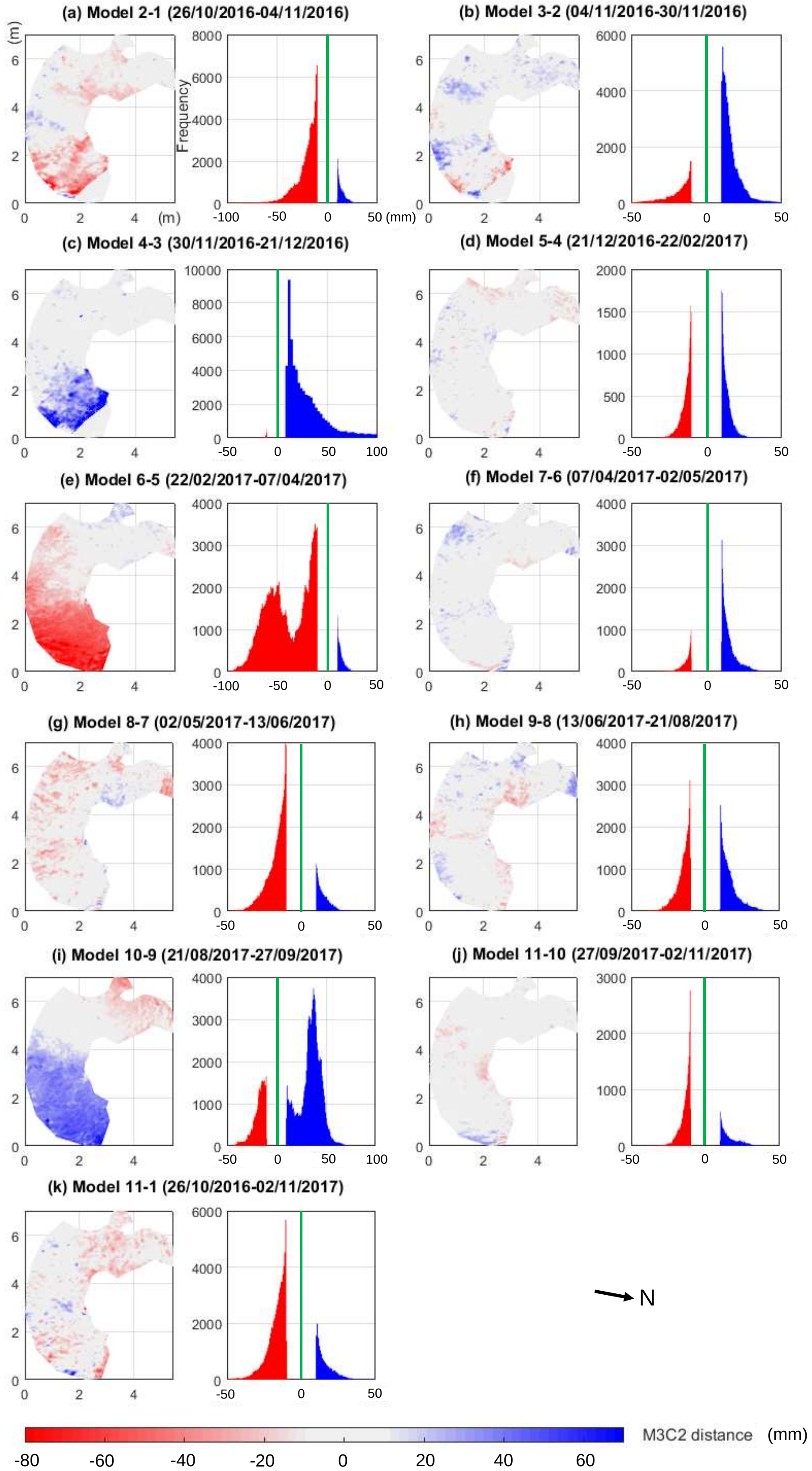

Figure 4. M3C2 distances and histograms over different survey intervals at both short-term (a–j) and long-term (k) scales for the Site 1 (hagg). Grey areas have non-significant changes.

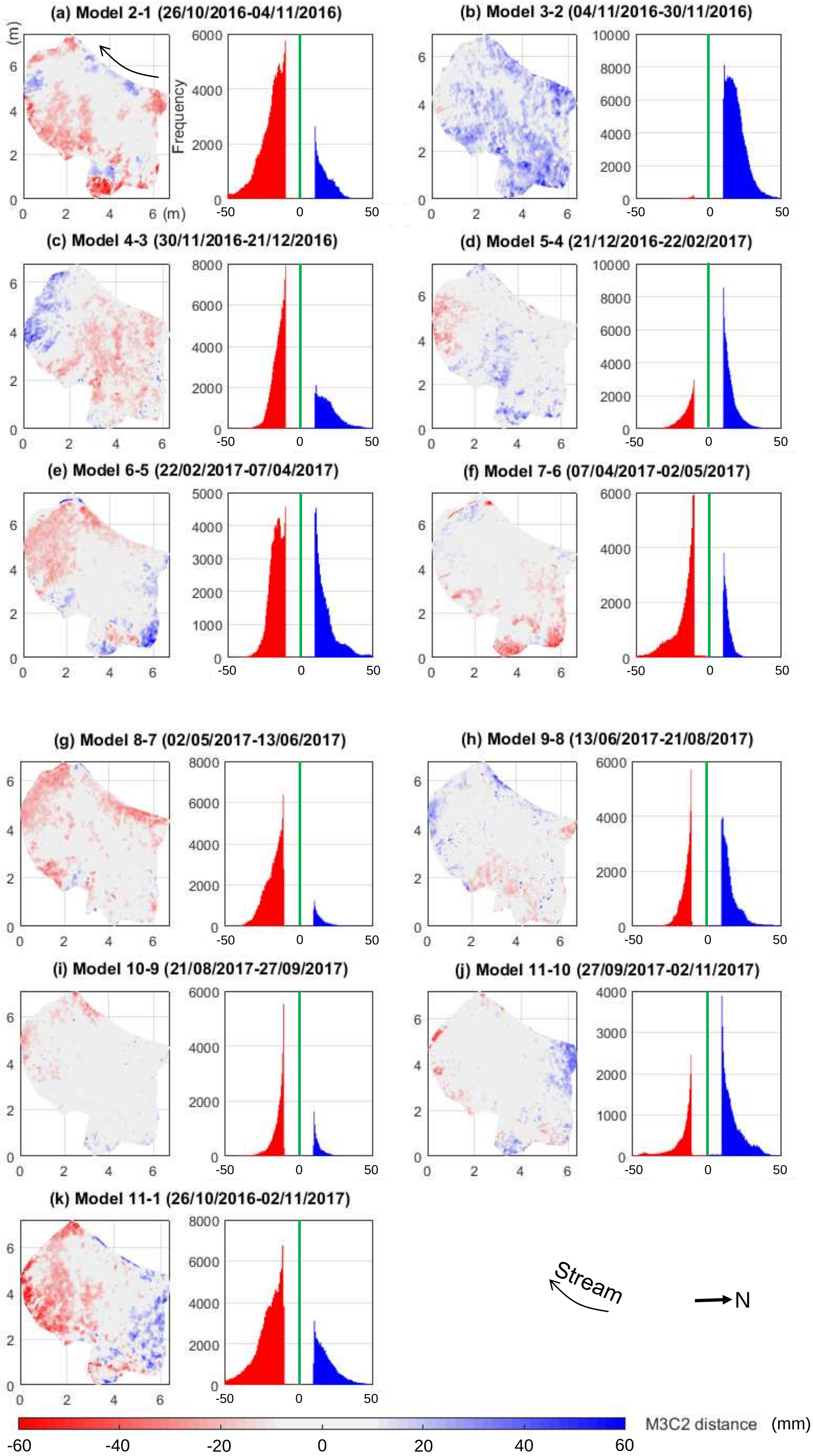

Figure 5. M3C2 distances and histograms over different survey intervals at both short-term (a–j) and long-term (k) scales for the Site 2 (gully wall). Grey areas have non-significant changes.

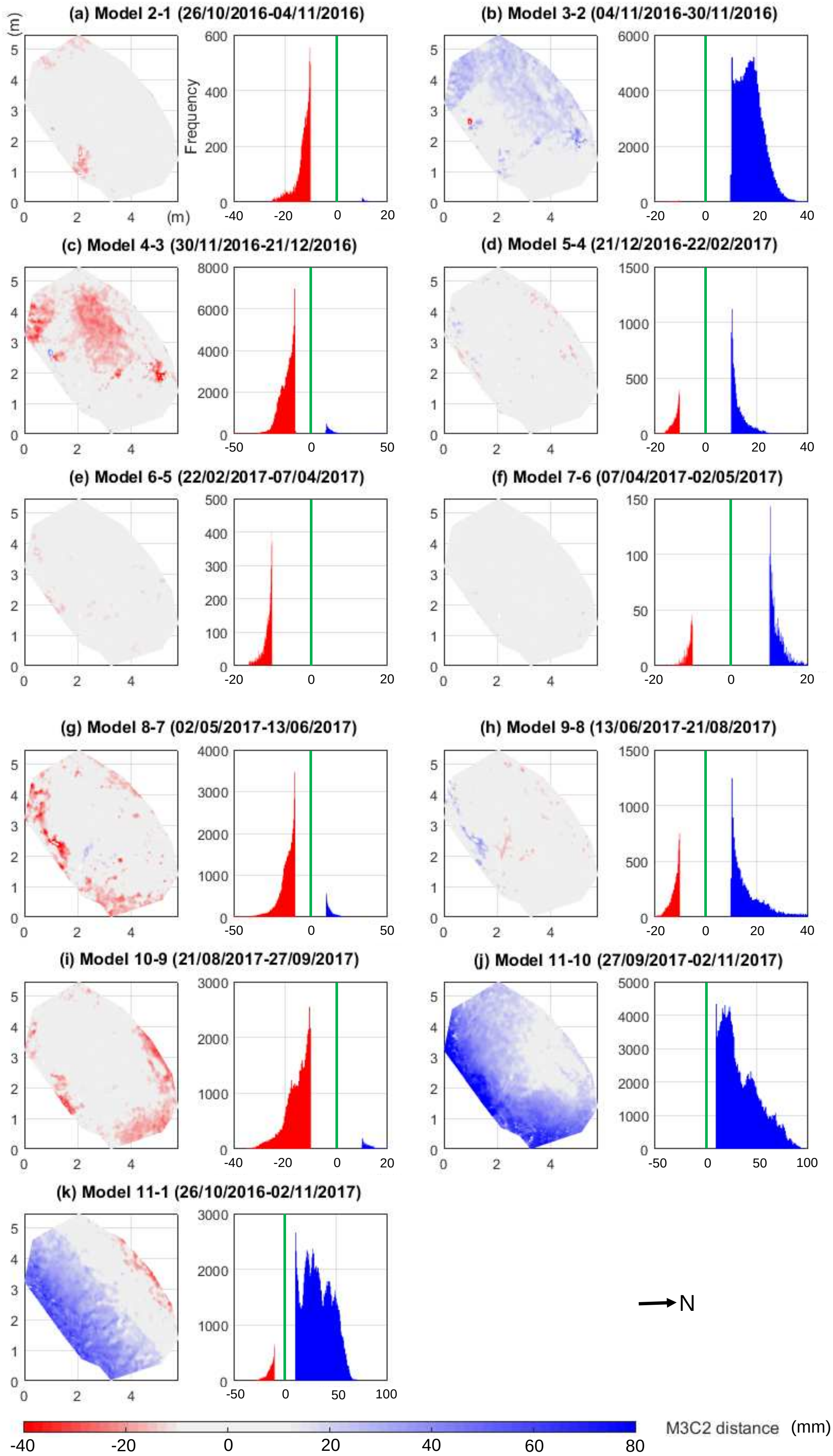

Figure 6. M3C2 distances and histograms over different survey intervals at both short-term (a–j) and long-term (k) scales for the Site 3 (riparian flat area). Grey areas have non-significant changes.

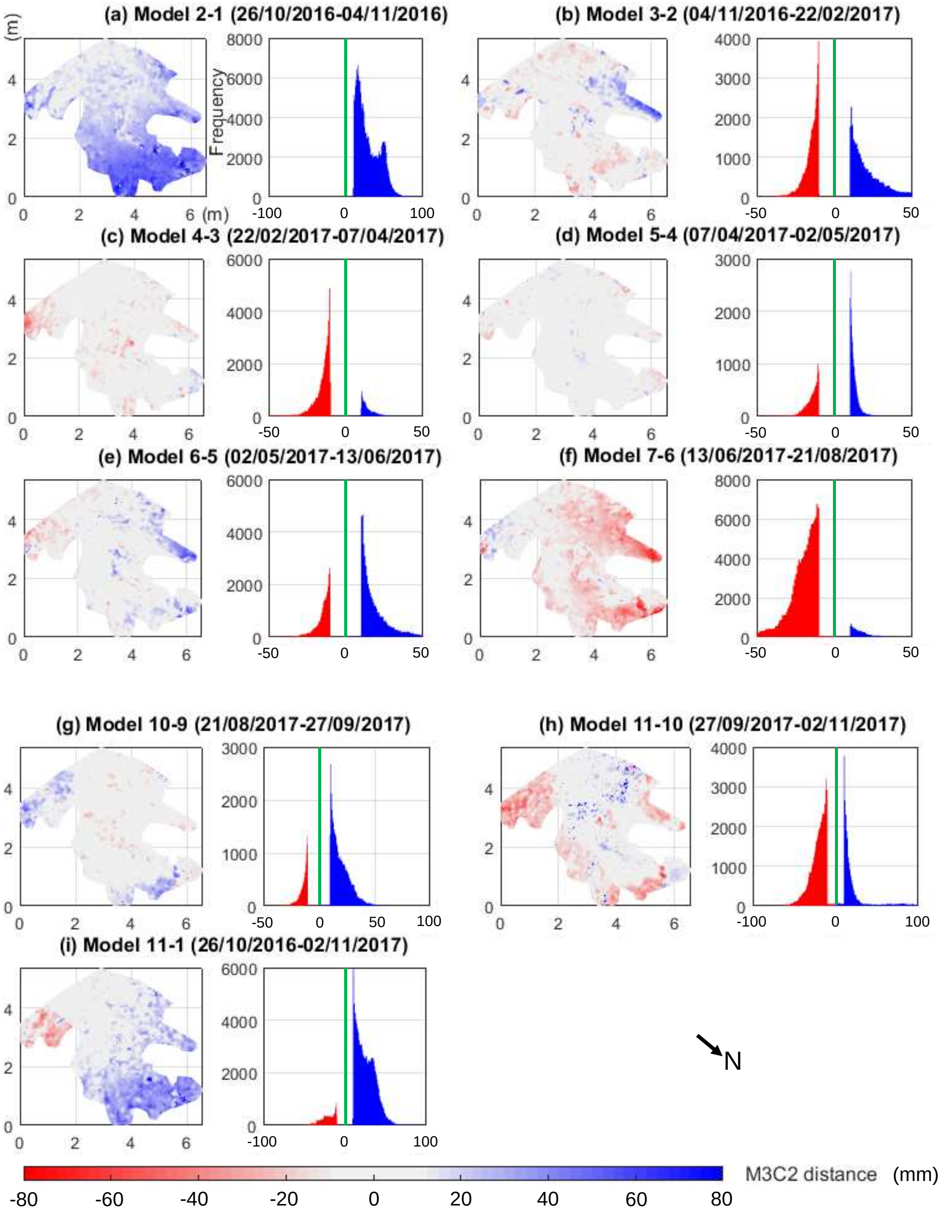

Figure 7. M3C2 distances and histograms over different survey intervals at both short-term (a–h) and long-term (i) scales for the Site 4 (gully head). Grey areas have non-significant changes.

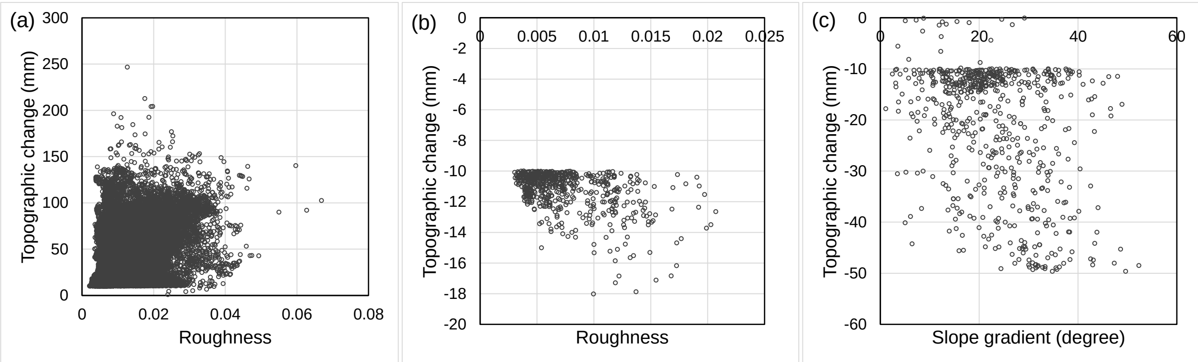

Figure 8. Relationships between topographic change and (a–b) roughness and (c) slope. The results were derived from models of (a) Site 1: 4–3; (b) Site 3: 7–6; (c) Site 3: 3–2. Roughness was calculated from the dense points of the start of the survey interval.

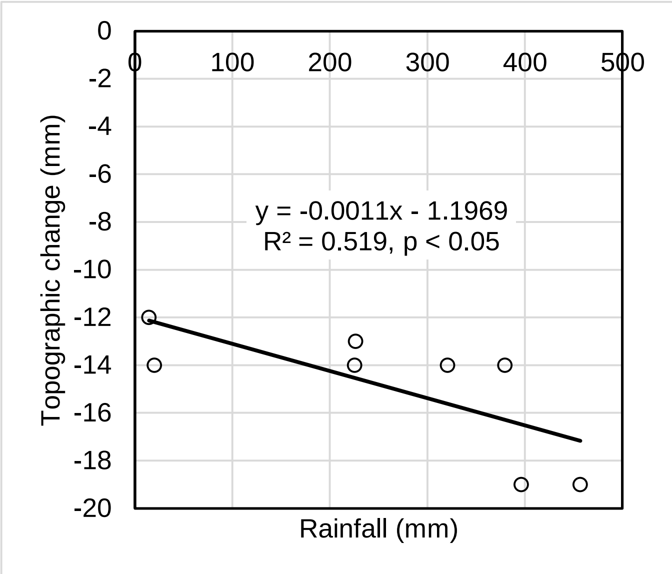

Figure 9. Relationships between topographic change and rainfall on Site 4 (gully head).

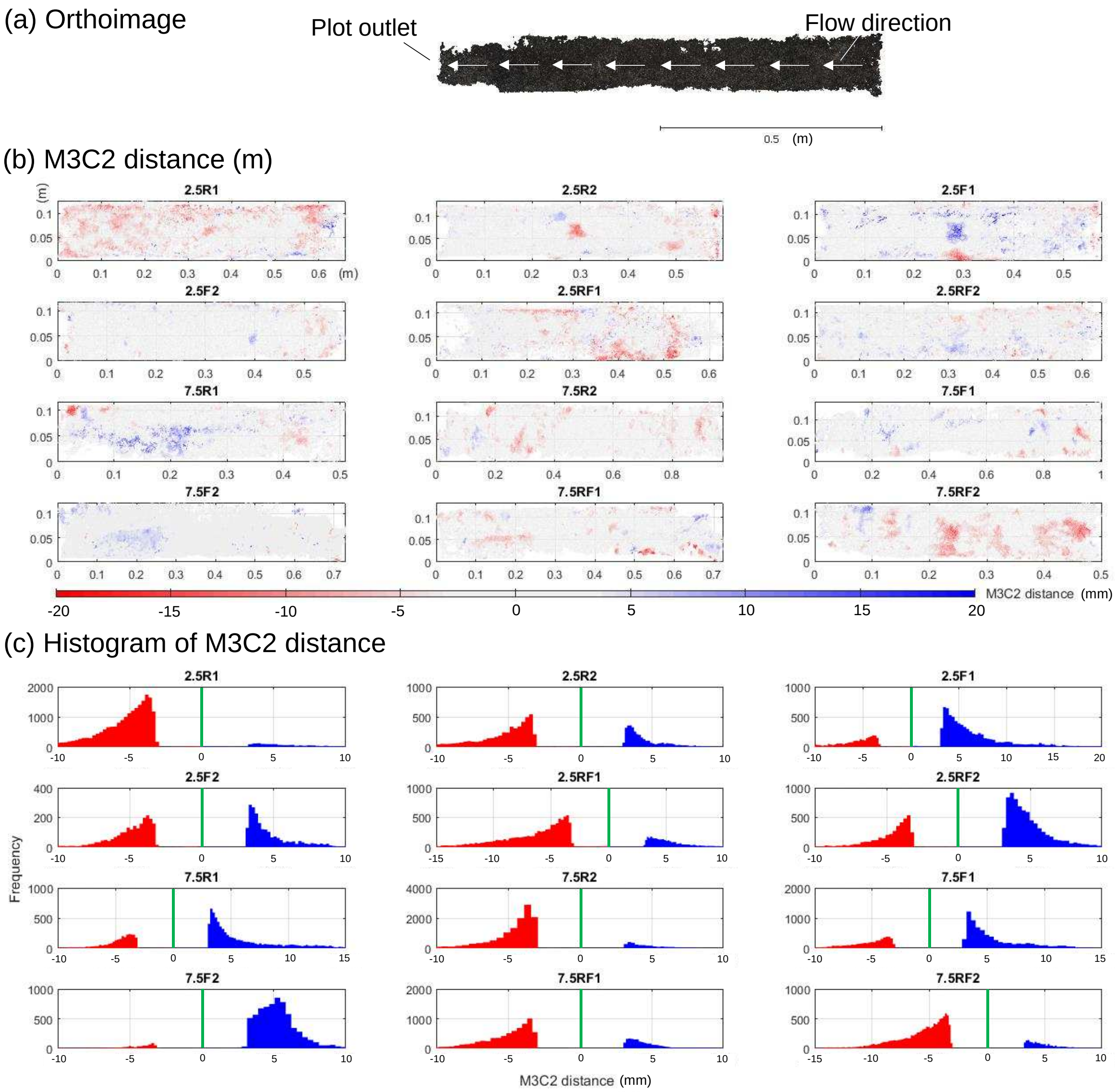

Figure 10. Spatial patterns of the significant M3C2 distances (a) and histogram of differences (b) at event scales for laboratory peat blocks. Grey areas have non-significant changes. Two slopes (2.5° and 7.5°), three treatments including Rainfall (R), Inflow (F) and Rainfall + Inflow (RF) and two replicates for each (1 and 2) were examined.

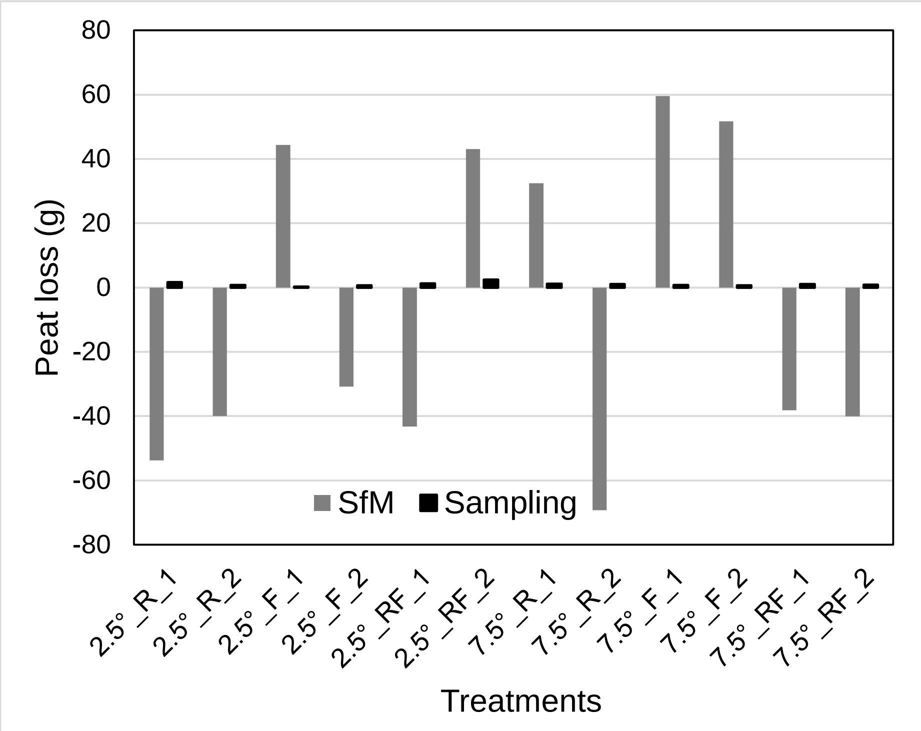

Figure 11. Summary of peat loss measured by sampling method and SfM techniques for the three treatments (Rainfall, Inflow and Rainfall + Inflow). Positive values show erosion while negative values show deposition. Two slopes (2.5° and 7.5°), three treatments including Rainfall (R), Infl ow (F) and Rainfall + Inflow (RF) and two replicates for each (1 and 2) were examined.

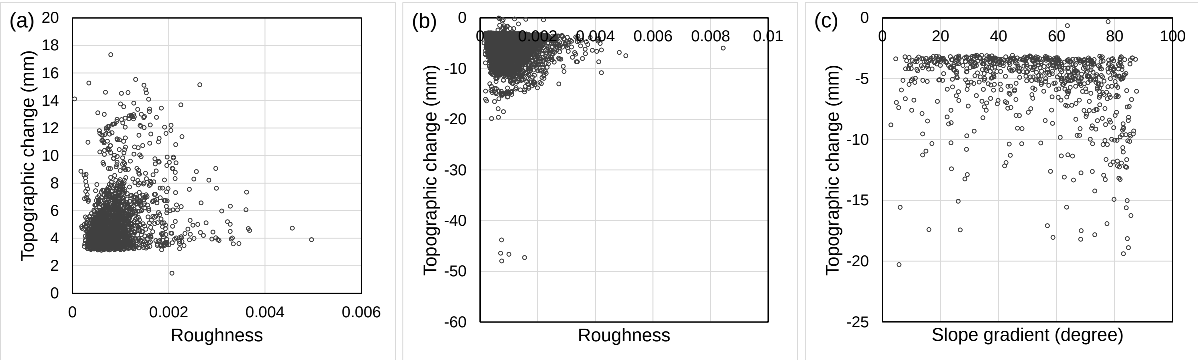

Figure 12. Relationships between topographic change and (a–b) roughness and (c) slope. The results were derived from models of (a) 7.5RF2; (b) 7.5R2; (c) 7.5F2. Roughness was calculated from the dense points of the start of the survey interval.

Graphical abstract

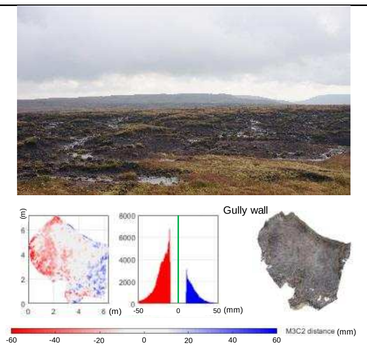

We present field and laboratory observations of peat erosion using Structure-from-Motion (SfM) photogrammetry. Over a 12 month period, 11 repeated SfM surveys were conducted on four geomorphological sites of 18–28 m^2 (peat hagg, gully wall, riparian area and gully head) in a blanket peatland in northern England. The spatial and temporal patterns of topographic change and its topographic controls were illustrated from both field and laboratory surveys.